

Structure-Guided Processing Path Optimization with Deep Reinforcement Learning

JOHANNES DORNHEIM¹, LUKAS MORAND², SAMUEL ZEITVOGEL¹, TAREK IRAKI¹, NORBERT LINK¹ AND DIRK HELM².

¹Intelligent Systems Research Group ISRG, Karlsruhe University of Applied Sciences, Karlsruhe, Germany (e-mail: {johannes.dornheim, samuel.zeitvogel, tarek.iraki, norbert.link}@hs-karlsruhe.de)

²Fraunhofer Institute for Mechanics of Materials IWM, Freiburg, Germany (e-mail: {lukas.morand, dirk.helm}@iwm.fraunhofer.de)

Corresponding author: Johannes Dornheim (e-mail: johannes.dornheim@hs-karlsruhe.de).

The authors would like to thank the German Research Foundation (DFG) for funding the presented work, which was carried out within the research project number 415804944: 'Tailored Material Properties via Microstructure Optimization: Machine Learning for Modelling and Inversion of Structure-Property-Relationships and the Application to Sheet Metals'. Also, we would like to thank Jan Pagenkopf for providing the crystal plasticity routine on which the implemented material model is based.

ABSTRACT A major goal of material design is the inverse optimization of processing-structure-property relationships. In this paper, we propose and investigate a deep reinforcement learning approach for the optimization of processing paths. The goal is to find optimal processing paths in the material structure space that lead to target structures, which have been identified beforehand to yield desired material properties. The contribution completes the desired inversion of the processing-structure-property chain in a flexible and generic way. As the relation between properties and structures is generally nonunique, typically a whole set of goal structures can be identified, that lead to desired properties. Our proposed method optimizes processing paths from a start structure to one of the equivalent goal-structures. The algorithm learns to find near-optimal paths by interacting with the structure-generating process. It is guided by structure descriptors as process state features and a reward signal, which is formulated based on a distance function in the structure space. The model-free reinforcement learning algorithm learns through trial and error while interacting with the process and does not rely on a priori sampled processing data. We instantiate and evaluate the proposed method by optimizing paths of a generic metal forming process to reach near-optimal structures, which are represented by one-point statistics of crystallographic textures.

INDEX TERMS Microstructure Evolution, Process Design, Inverse Material Design, Deep Reinforcement Learning, Multi Goal Reinforcement Learning, Reward Shaping, PSP Linkages, ICME, Crystal Plasticity, Crystallographic Texture

I. INTRODUCTION

Manufacturing processes produce materials with desired properties by generating the corresponding, underlying material structures. The relations between processing, structure, property, and performance of materials are represented in [1] from a production point of view as a three-link chain. The inversion of this three-link chain model, as depicted in Figure 1, reveals a workflow for the design of new materials and processes, driven by the desired properties and performance of the material. The present paper focuses on the last link of the inverted model: The identification of optimal processing

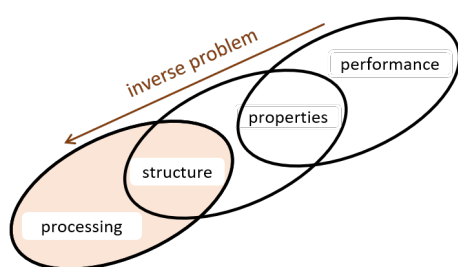


FIGURE 1. Three-link chain, following [1]. Orange shaded chain: Focus of this publication.

paths in a given multi-step manufacturing process aiming to produce predefined structures. A deep reinforcement learning approach is proposed for optimal path-finding, which is guided by a reward function defined in the native space of the material structures. The method is generic for any set of goal structures and therefore independent of specific target properties and property types, as long as the material structure is correlated to the target properties.

A material property usually has a one-to-many relation to structures, which means that a set of structures is equivalent with respect to the desired material properties. The aim of processing path optimization is then to find a path from an initial structure to one of the equivalent target structures. In the present contribution, we propose an algorithm to find optimal paths to a single target structure and an extended algorithm to solve problems with multi-equivalent target structures. The contribution of *structure-guided processing path optimization* to the inverse optimization of processing-structure-property relationships is depicted in Figure 2. The theory of the following sections and methods proposed in this publication apply to structures of all scales. Microstructures are of special interest in the material design context. Therefore, we focus on microstructure processing use-cases. In the following, we use the term microstructure without loss of generality.

The proposed method is instantiated and evaluated with a synthetic metal forming sample process. The process consists of a sequence of forming steps, where a uniaxial displacement is applied to the material with a certain direction and magnitude being chosen by the algorithm at each step. We simulate the evolution of crystallographic texture as one of the major microstructural features that is affecting macroscopic material properties. In process-integrated online reinforcement learning the reinforcement agent directly interacts with the process: The optimization algorithm obtains the current crystallographic texture and determines the next deformation step during the process execution. The proposed algorithm can be set in series to any method for inverse structure-property mappings. Recent examples of such methods in metal forming are described for example in [2], [3]. The core of both approaches is a supervised learning-based identification scheme for regions in microstructure space yielding a set of optimal or near-optimal microstructures with respect to given target properties.

A. RELATED WORK

A general approach for materials design and optimal processing is described by the *Microstructure Sensitive Design* (MSD) framework, which goes back to the publication of Adams *et al* [4]. An extensive review of publications in the context of the MSD framework and its applications can be found in Fullwood *et al* [5]. Central to MSD is the description of microstructures using n -point correlation functions transformed into a spectral representation. After this transformation, microstructures are defined by single points in high-dimensional spectral space and the set of microstruc-

tures obtaining specific target properties can be identified in the form of points lying on iso-property hyperplanes. The overall framework of MSD is described in [5] as a seven-step process starting from the definition of the principal properties (step one) and ending with the identification of processing paths to reach a target microstructure from a given starting microstructure (step seven). While a huge corpus of publications exists for the first steps, only a few publications can be found focusing on processing path optimization in the context of material design [6]–[12]. Following the MSD approach, in [6], a so-called *texture evolution network* is built based on a priori sampled processing paths. The *texture evolution network* is a directed tree graph with crystallographic textures as vertices and process steps as edges. Once the graph is built, it is mapped to property space by a structure-property mapping. In property space, graph search algorithms are used to find processing paths from a given graph-node (which is denoting the starting structure) to a target-node (which is denoting a structure with desired properties). The sequence of edges passed is then the aimed processing path. In [8], crystallographic texture evolution models for the three processes of rolling, of uniaxial tension, and of compression are used to create a network in the space of microstructures, consisting of processing-streamlines. Linear differential transition functions are derived from the continuity equation (following [13]) and are used to describe the microstructure evolution for each process. Like the texture evolution networks the a priori calculated streamlines can be used as a process evolution model and search algorithms can be used to query the model. In [9], one-step deformation processes are optimized to reach an element of a set of target microstructures. Tension, compression, and various shear processes are represented by so-called *process planes*, per process principal component analysis (PCA) projections of microstructures that are reachable by the specific process. The optimization is performed by searching for the process plane which best represents one of the target microstructures. In [10] this approach is extended by calculating PCA projections also for two- and three-step processes. In [11] variational autoencoders are used to represent processed microstructures in a lower-dimensional space. A priori sampled microstructures with associated processing paths are stored in a database. For a given target microstructure, microstructures with known processing paths are then identified in the database by using a distance-function defined in the low-dimensional space. The method is applied to a data set, sampled from parametrized shear, rolling, and tension processes with up to four process steps. [12] combines Bayesian optimization and kinetic Monte Carlo simulations to optimize welding process parameters and a grain growth process with the objective defined in the microstructure space.

The majority of the methods discussed above are based on a search-algorithm, either directly searching in a set of a priori sampled processing paths [6], [9]–[11] or in a generalized structure derived from a priori processing paths [7], [8]. Thereby, they implicitly rely on the assumption, that the

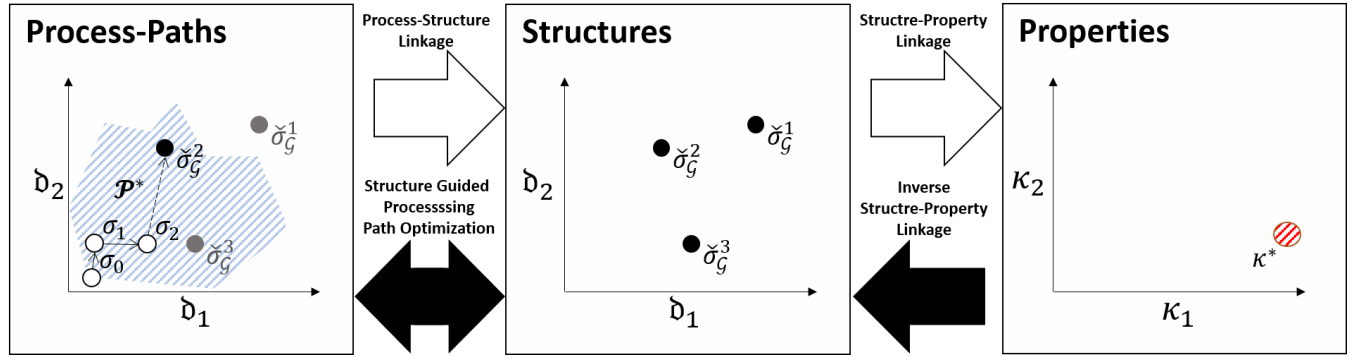


FIGURE 2. Overview of *structure-guided processing path optimization* in the context of inverse structure-property mappings. The direct three-link chain (Processes-Structures-Properties) is depicted by white arrows; its inversion by black arrows. Goal-properties κ^* are mapped to a set of target structures $\check{\sigma}_G^g \in \mathcal{G}$. Structures σ are described by features $\mathbf{d}(\sigma)$. For a given initial structure σ_0 , the aim of *structure-guided processing path optimization* is then to find an efficient sequence of processing steps to one of the target structures from \mathcal{G} . As indicated by the shaded process-area in the structure feature-space, not all structures from \mathcal{G} are necessarily reachable by the process. The optimization is guided by the structure features and a reward function defined in the space of structures.

sampled set is representative and fully describes the structure space. In contrast, [12] actively samples a process simulation. When it comes to the process-path length, most of the algorithms optimize single-step processes [9], [12] or processes with only few processing-steps (up to six processing-steps) [10], [11]. Except for [9], [10], the discussed methods do not explicitly consider the existence of sets of equivalent microstructure solutions for a specified property goal.

B. CONTRIBUTION

We propose a model-free deep reinforcement learning algorithm for *structure-guided processing path optimization* and an extended algorithm for sample-efficient processing path optimization in the case of various equivalent target microstructures. The proposed algorithms can optimize processing paths of arbitrary length (in our application study we evaluate on paths with up to 100 processing-steps). The proposed algorithms are not tied to a specific process model and do not need a priori samples. Instead, they query the process simulation during optimization (online). Online algorithms are not restricted to the information which is represented in a priori sampled datasets and particularly sample from regions that are frequently visited during optimization. This usually has a positive impact on sample-efficiency and the quality of optimization results [14].

Amongst others, reinforcement learning has been proposed for model-free optimal control of various non-linear manufacturing processes like polymerization reaction systems [15], laser welding [16] and deep drawing [17]. The algorithms proposed in this paper are based on *deep Q networks* (DQN) [18] with several enhancements [19]–[21]. We extend DQN by a goal-prioritization and data-augmentation mechanism to exploit the fact that several target microstructures are equivalent regarding the objective. The basis for these extensions is the generalization of the reinforcement learning value functions to include the target microstructures, as it is done in the *universal value function approximator* approach [22]. The data-augmentation mechanism we propose

is inspired by *hindsight experience replay* [23]. We utilize *potential based reward shaping* [24] for sample-efficient learning.

The contribution of this paper is four-fold:

- (1) The proposition of a deep reinforcement-learning algorithm to solve single target *structure-guided processing path optimization* problems.
- (2) The extension of the proposed single target algorithm to a novel deep reinforcement-learning algorithm to efficiently solve multi-equivalent goal optimization problems.
- (3) The proposition of a histogram-based distance-function for orientation densities to describe the crystallographic texture
- (4) An extensive quantitative evaluation of our algorithms on a generic metal forming process.

To evaluate the proposed methods, we use an efficient mean-field crystal plasticity model of Taylor type for the study presented in this paper. The target of the optimized process is the crystallographic texture in a single-phase polycrystalline material. However, due to the generic nature of our method, it can also be combined with more accurate but computationally expensive full-field simulation approaches, see for example [25], [26]. Furthermore, it is not restricted to optimize crystallographic texture but can be applied to any kind of microstructural or material quantity.

To guarantee the reproducibility of our results and to encourage the development of *structure-guided processing path optimization* methods, we publish the used simulation wrapped by an openAI Gym [27] reinforcement learning environment.

C. PAPER STRUCTURE

This paper is structured as follows: In the following Section, II we introduce the fundamental basics of the reinforcement learning approach and the material model used for our evaluation case-study. Then, in Section III our proposed algorithms for single-target and multi-equivalent-target *structure-*

TABLE 1. Table of the most important symbols used throughout the paper

Symbol	Quantity
Reinforcement Learning	
S	State-Space, Set of states s
A	Action-Space, Set of actions a
$t \in \mathbb{N}$	time-step within an episode
$K \in \mathbb{R}^+$	Maximum length of episode/Processing path
$P(s_{t+1} s_t, a_t)$	probability of the transition to s_{t+1} when taking a_t in s_t
$R(s_t, a_t, s_{t+1})$	Reward for the transition from s_t to s_{t+1} via a_t
$\gamma \in [0, 1]$	Discount factor
π, π^*	(possibly stochastic) control policy, optimal π
$\mathcal{V}_\pi : S \rightarrow \mathbb{R}$	Expected future reward for π
$\mathcal{V}^* : S \rightarrow \mathbb{R}$	Expected future reward for π^*
$\mathcal{Q}^* : S \times A \rightarrow \mathbb{R}$	Expected future reward for π^*
x	Experience tuple (s_t, a_t, s_{t+1}, R)
\mathcal{D}	Replay Memory, consisting of experience tuples x
$\alpha \in [0, 1]$	Q-Learning Learning Rate
θ, θ^-	Function approximation weights
Application	
\mathcal{S}	Space of microstructures $\sigma, \sigma_t, \sigma^*$
\mathcal{K}	Space of material properties κ
\mathcal{P}	Process path
\mathcal{P}^*	Optimal process path
\mathcal{G}	Set of equivalent target microstructures $\check{\sigma}_G$
$\mathcal{S}_P \subseteq \mathcal{S}$	Reachable Microstructures
$d_\sigma : \mathcal{S} \times \mathcal{S} \rightarrow \mathbb{R}$	microstructure distance-function
$f(h)$	Orientation Density Function
Taylor Model	
$T^{(i)}$	Cauchy stress of i th crystal
\mathbf{F}	Deformation gradient
\mathbf{L}	Velocity gradient
\mathbf{R}	Rotation matrix
E	Young's modulus

guided processing path optimization are described. Section IV describes the application case study that is used to evaluate our methods. In Section V, evaluation results are reported. Finally, the research results are summarized and discussed in Section VI.

II. BACKGROUND

A. MARKOV DECISION PROCESS AND DYNAMIC PROGRAMMING

Markov decision processes (MDP) are defined by the 5-tuple (S, A, P, R, γ) and build the formal basis of the problem definition for the algorithms of reinforcement learning and of dynamic programming. S is the set of all states s of the system, and A is the set of allowed control actions a . $P(s_{t+1}|s_t, a_t)$ is the probability of transition to the successor state s_{t+1} when applying action a_t in state s_t . Due to the Markov property, the one-step transition probability function P is sufficient to completely describe the transition dynamics of the decision process. $R(s_t, a_t, s_{t+1})$ is the reward function, delivering a real-valued reward signal, when a transition from s_t to s_{t+1} takes place, triggered by action a_t at time step t . The discount factor $\gamma \in [0, 1]$ is the degree of future reward discounting.

For a given control policy π , a possibly stochastic mapping from states to actions $A \sim \pi(S)$ and the time-index t , the

state value function

$$\mathcal{V}_\pi(s_t) = \mathbb{E}_{P, \pi} \left[R(s_t, a_t, s_{t+1}) + \gamma \mathcal{V}_\pi(s_{t+1}) \right], \quad (1)$$

denotes the expected discounted future reward when applying the control policy π from state s_t onwards, where $a_t \sim \pi(s_t)$ and s_{t+1} is drawn according to P . The MDP is considered to be solved when an optimal control policy π^* is found, for which the expected future reward is maximized:

$$\pi^*(s) = \arg \max_{a \in A} \mathbb{E}_P \left[\mathcal{V}^*(s') \right], \quad (2)$$

for all $s \in S$, where $\mathcal{V}^* = \mathcal{V}_{\pi^*}$. As it can be seen in (2), π^* can be extracted from \mathcal{V}^* . Consequently, finding π^* is equivalent to finding \mathcal{V}^* . When the transition function P is known in advance, \mathcal{V}^* can be determined by *dynamic programming* methods.

B. DEEP REINFORCEMENT LEARNING

If the transition function P is not known, methods from reinforcement learning can be used to find the optimal policy in an iterative *learning-by-doing* fashion, by interacting with the processes and, based on the experiences made, deriving the optimal policy π^* . In function-based reinforcement learning, expected future reward functions, like the value function (1), are modeled and the model is used to solve the MDP. The objective of Q-learning based methods is to identify the optimal Q-function \mathcal{Q}^* , also named *state-action value function*:

$$\mathcal{Q}^*(s_t, a_t) = \mathbb{E}_P \left[R(s_t, a_t, s_{t+1}) + \gamma \mathcal{Q}^*(s_{t+1}, \pi^*(s_{t+1})) \right]. \quad (3)$$

Unlike the value function from (1), the Q-function captures the one-step system dynamics by taking the actions into account. In Q-Learning, the approximation of the optimal Q-function is updated based on experience-tuples $x_t = (s_t, a_t, s_{t+1}, R(s_t, a_t, s_{t+1}))$ gathered in each time-step by interacting with the process. The update is as follows:

$$\mathcal{Q}'(s_t, a_t) \leftarrow \mathcal{Q}(s_t, a_t) + \alpha(\delta_{\mathcal{Q}}(x_t)), \quad (4)$$

where $\alpha \in [0, 1]$ is the Q-learning rate and $\delta_{\mathcal{Q}}(x_t)$ is the *time difference error*, defined by

$$\begin{aligned} \delta_{\mathcal{Q}}(x_t) &= R(s_t, a_t, s_{t+1}) \\ &+ \gamma \max_{a_{t+1} \in A} \mathcal{Q}(s_{t+1}, a_{t+1}) - \mathcal{Q}(s_t, a_t). \end{aligned} \quad (5)$$

The Q-function is guaranteed to converge to \mathcal{Q}^* if the explorative policy, which is used during learning guarantees that the probability of taking an action a in state s is non-zero for every $(s, a) \in S \times A$ [28]. Often an ϵ -greedy policy is used for this purpose, which acts randomly in an ϵ fraction of time-steps and greedy (according to the current Q-function estimation) in all other cases [14].

Pure Q-learning (without function approximation) is subject to the *curse of dimensionality*, like other algorithms from reinforcement learning and dynamic programming. This is leading to difficulties in terms of the data complexity required for sampling high dimensional state-action spaces.

To overcome these difficulties, in real-world applications, Q-learning is often combined with supervised learning of an approximation of the Q-function. When artificial neural networks are used for function approximation, the Q-function update learning rate α is dropped in favor of the back-propagation optimizer learning rate. The training target for a specific experience-tuple x_t is then

$$Y_Q = R(s_t, a_t, s_{t+1}) + \gamma \max_{a_{t+1} \in A} Q(s_{t+1}, a_{t+1}, \theta), \quad (6)$$

where $Q(s, a, \theta)$ is the Q-function approximation, represented by an artificial neural network with weights θ . It is important to note that the theoretical convergence guarantees from pure Q-learning cease to hold when function approximators are used.

In this paper we use the *deep Q Networks* (DQN) algorithm [18] as the core reinforcement learning algorithm. DQN combines Q-function approximation using a deep artificial neural network with *experience replay* [29]. In typical reinforcement learning tasks, successive states in the process trajectory are highly correlated. Due to this fact, updating the artificial neural network weights in the order of incoming experiences x_t breaks the i.i.d. assumption and leads to a phenomenon called *catastrophic forgetting*: Early experiences that may become useful later on in the training process are buried under later experiences. Experience replay addresses this, by storing the experiences in a so-called *replay memory* $\mathcal{D} = [e_0, e_1, \dots, e_N]$ which is used to sample data for mini-batch updates of the DQN in a stochastic fashion during learning. Due to the dependency of training targets on the approximated Q-function with constantly updated parameters θ as shown in (6), learning can still be unstable. In DQN, *target-parameters* θ^- , used for target-calculations, are therefore decoupled from *online-parameters* θ , which are continuously updated and used to derive the explorative policy π . The target-parameters are kept fixed for n_θ steps and are then updated by copying the online-parameters $\theta^- \leftarrow \theta$. The per-sample training target is then

$$Y_{DQN} = R(s_t, a_t, s_{t+1}) + \gamma \max_{a_{t+1} \in A} Q(s_{t+1}, a_{t+1}, \theta^-). \quad (7)$$

Further DQN enhancements have been shown to improve learning performance and stability. The enhancements we employ are *prioritized experience replay* (PER) [19], *double Q-learning* [20] and *dueling Q-learning* [21]. In standard DQN, experiences are sampled uniformly from the replay memory \mathcal{D} to form mini-batches for network training. As the name PER suggests, some experiences are prioritized during sampling. PER is based on the assumption that experiences with a higher time-difference error δ_Q hold more information regarding the optimization task. To ensure that the prioritization does not lead to a loss of diversity in the training data, PER uses a stochastic prioritization. The PER hyperparameter $\alpha_{PER} \in \mathbb{R}_0^+$ determines the influence of the prioritization, where $\alpha_{PER} = 0$ corresponds to uniform sampling. Any deviation from uniform sampling is in conflict with the i.i.d. assumption of supervised learning. In RL

this becomes noticeable especially towards the end of the learning process. The resulting bias is corrected in PER by using *weighted importance-sampling*. The amount of initial importance sampling correction β is specified by a second PER hyperparameter β_0 and then linearly approaches 1.0 during training. For an in-depth explanation of the stochastic prioritization and importance sampling, we refer to [19].

When using Q-function approximation, the maximization over estimated action values in the calculation of δ_Q (5) can lead to an systematic overestimation of expectation values [30]. *Double Q-learning* [20] reduces such overestimation by decoupling the maximization of the action value from the action evaluation. The maximization is then done by the online-network, while the evaluation is still conducted by the network with the target parameters. The resulting per-sample target is

$$Y_{DDQN} = R + \gamma Q(s_{t+1}, \arg \max_{a_{t+1} \in A} Q(s_{t+1}, a_{t+1}, \theta), \theta^-), \quad (8)$$

where $R = R(s_t, a_t, s_{t+1})$.

In *Dueling Q-learning* a decomposition of the Q-network architecture into two separate streams is proposed. The decomposition is based on the relationship $Q_\pi(s, a) = \mathcal{V}_\pi(s), \mathcal{A}_\pi(s, a)$, where \mathcal{V}_π is the state-value function from (1) and \mathcal{A}_π is the so-called advantage-function, the delta of the value of a given state s and the value of applying action a in s . Dueling Q-learning is compatible with PER and *double Q-Learning*. For details we refer to [21].

C. TAYLOR-TYPE MATERIAL MODEL

For the purpose of this work, a Taylor-type crystal plasticity model is used as is described in [31]. The Taylor-type model is based on the assumption that all crystals in a polycrystalline aggregate experience the same deformation and does not consider spatial relations and morphological texture. In addition to the classical Taylor model, the stress response of the material is given by the average volume-weighted stress over all n crystals

$$\bar{\mathbf{T}} = \frac{1}{V} \sum_{i=1}^n \mathbf{T}^{(i)} V^{(i)}, \quad (9)$$

where \mathbf{T} denotes Cauchy stress. Based on the multiplicative decomposition of the deformation gradient in its elastic and plastic parts $\mathbf{F} = \mathbf{F}_e \cdot \mathbf{F}_p$, the stress tensor in the intermediate configuration can be derived for a single crystal:

$$\mathbf{T}^* = \frac{1}{2} \mathbb{C} : (\mathbf{F}_e^T \cdot \mathbf{F}_e - \mathbf{I}), \quad (10)$$

where \mathbf{I} is the second order identity tensor, \mathbb{C} is the fourth order elastic stiffness tensor, and the $:$ operator stands for the double dot product. For cubic symmetry, \mathbb{C} has only three independent parameters: C_{11} , C_{12} , and C_{44} . For iron single crystals, these can be set to 226.0, 140.0, and 116.0 GPa, respectively [32]. The evolution of the plastic deformation is

defined on the basis of the plastic part of the velocity gradient \mathbf{L}_p :

$$\mathbf{L}_p = \dot{\mathbf{F}}_p \cdot \mathbf{F}_p^{-1}. \quad (11)$$

The flow rule is defined as the sum of the shear rates $\dot{\gamma}$ on every active slip system η [33]:

$$\mathbf{L}_p = \sum_{\eta} \dot{\gamma}^{(\eta)} \mathbf{m}^{(\eta)} \otimes \mathbf{n}^{(\eta)}. \quad (12)$$

The slip systems are defined via the slip plane normal \mathbf{n} and the slip direction \mathbf{m} . For body-centered cubic crystals, the slip systems are given by the Miller indices $\{110\}<111>$ and $\{112\}<111>$. For simplicity and with adequate accuracy, the slip system family $\{123\}<111>$ is not incorporated. To solve (12), a phenomenological approach is used. The shear rates are given by the power-law as it is described for example in [34]:

$$\dot{\gamma}^{(\eta)} = \dot{\gamma}_0 \left| \frac{\tau^{(\eta)}}{r^{(\eta)}} \right|^{1/m} \text{sign}(\tau^{(\eta)}), \quad (13)$$

where $r^{(\eta)}$ is the slip system resistance, and $\dot{\gamma}_0$ and m stand for the reference shear rate and the rate sensitivity and are set to 0.001 sec^{-1} and 0.02 , respectively [35]. The resolved shear stress $\tau^{(\eta)}$ is defined by Schmid's law

$$\tau^{(\eta)} = ((\mathbf{F}_e^T \cdot \mathbf{F}_e) \cdot \mathbf{T}^*) : (\mathbf{m}^{(\eta)} \otimes \mathbf{n}^{(\eta)}). \quad (14)$$

To model the hardening behavior, a description is used that can be found for example in [36] and [37]. The hardening model is of an extended Voce-type [38]:

$$\hat{\tau}^{(\eta)} = \tau_0 + (\tau_1 + \vartheta_1 \Gamma)(1 - e^{-\Gamma \vartheta_0 / \tau_1}), \quad (15)$$

in which τ_0 , τ_1 , ϑ_0 , and ϑ_1 are material dependent parameters that are calibrated to experimental data of DC04 steel¹ and therefore set to 90.0 , 32.0 , 250.0 , and 60.0 MPa , respectively. The accumulated plastic shear Γ is given by

$$\Gamma = \int_0^t \sum_{\eta} \left| \dot{\gamma}^{(\eta)} \right| dt. \quad (16)$$

The evolution of the slip system resistance can be calculated via

$$\dot{r}^{(\eta)} = \frac{d\hat{\tau}^{(\eta)}}{d\Gamma} \sum_{\zeta} \hat{q}_{\eta\zeta} |\dot{\gamma}^{(\zeta)}|, \quad (17)$$

where $\hat{q}_{\eta\zeta}$ is a matrix that describes the ratio between latent and self-hardening. Having two slip system families, then $\hat{q}_{\eta\zeta}$ is composed out of the parameters \hat{q}_1 and \hat{q}_2 , while the diagonal elements are equal to 1.0 . \hat{q}_1 represents the latent hardening of coplanar slip systems and \hat{q}_2 of non-coplanar slip systems. Both values are set to 1.4 [34].

¹experiments performed at IUL Dortmund during DFG project Graduate School 1483 [39]

D. REPRESENTATION OF CRYSTALLOGRAPHIC TEXTURE AS A MICROSTRUCTURAL FEATURE

In this work, the crystallographic texture is described by a one-point correlation function, namely the orientation distribution function (ODF). The ODF is commonly defined as a continuous and non-negative function $f(h)$ with

$$f(h)dh = \frac{V(h)}{V} \quad \text{and} \quad \int_{SO(3)} f(h)dh = 1, \quad (18)$$

where h is a point in $SO(3)$ and $V(h)$ is the volume of h in the orientation space. To describe the ODF of metallic materials, conditions for crystal and sample symmetry can be introduced. Due to these symmetry conditions, various regions of $SO(3)$ are equivalent. Therefore, orientations can be mapped to a fundamental zone, such that the ODF described by the mapped orientations $f(\tilde{h})$ is physically indistinguishable from $f(h)$ [40].

For function approximation in the context of reinforcement learning a low dimensional state-representation is preferred that describes the state adequately by ordered features. These requirements can be fulfilled by approximating the ODF using *generalized spherical harmonics* (GSH) [40] and taking its coefficients as state-representation. By embedding crystal and sample symmetry, the GSH can be symmetrized to reduce the number of necessary coefficients:

$$f(h) = \sum_{l=0}^{\infty} \sum_{u=1}^{M(l)} \sum_{v=1}^{N(l)} C_l^{uv} \dot{T}_l^{uv}(h), \quad (19)$$

where \dot{T}_l^{uv} are the symmetrized generalized harmonics functions and C_l^{uv} are the corresponding coefficients. $M(l)$ and $N(l)$ describe the number of linearly independent harmonics for the crystal and sample symmetry and are defined in [40]. (19) depicts an infinite series, which is usually truncated to a certain degree based on the application of interest. The obtained coefficients represent a compact and ordered set of features describing the ODF. Due to these properties, GSH coefficients are popular ODF descriptors in machine learning and data mining applications (e.g. [5], [6], [7], [10]). We denote the GSH coefficient vector of a texture σ with the crystal system Ω of grade l by $\zeta_l^{\Omega}(\sigma)$. The representation of the ODF via a vector of GSH coefficients does not allow the unambiguous calculation of distances between structures, which is a prerequisite to reach given target structures. An alternative representation will therefore be proposed in Section IV.

III. METHOD

A. OBJECTIVE

For a given target microstructure $\check{\sigma} \in \mathcal{S}$, *structure-guided processing path optimization* aims to find a sequence of processing steps $\mathcal{P}^* = (a_0, a_1, \dots, a_{n-1}, a_n)$, where $n < K$ and K is the maximum length of \mathcal{P} , that leads from an initial microstructure σ_0 to the nearest possible microstructure

$$\sigma^* = \arg \min_{\sigma \in \mathcal{S}_{\mathcal{P}}} d_{\sigma}(\sigma, \check{\sigma}), \quad (20)$$

from the set of microstructures $\mathcal{S}_P \subseteq \mathcal{S}$ which are reachable by the process, where $d_\sigma : \mathcal{S} \times \mathcal{S} \rightarrow \mathbb{R}_0^+$ is a distance function in the microstructure space \mathcal{S} . The optimal processing path \mathcal{P}^* is the shortest among all paths from σ_0 to σ^* . Neither \mathcal{S}_P nor σ^* are known in advance. Instead, an interactive microstructure changing process is given.

Typically multiple equivalent material microstructures exist, which all of them bear the desired material properties exactly or at least in a sufficiently small range. Approaches for the inversion of structure-property mappings therefore often return a set \mathcal{G} of target microstructures $\check{\sigma}_G \in \mathcal{G}$ instead of a single target microstructure $\check{\sigma}$ [2], [3]. The additional aim of processing path optimization is then to identify the best reachable target microstructure $\check{\sigma}_G^* \in \mathcal{G}$. (20) extends to

$$(\sigma^*, \check{\sigma}_G^*) = \arg \min_{(\sigma, \check{\sigma}_G) \in \mathcal{S}_P \times \mathcal{G}} d_\sigma(\sigma, \check{\sigma}_G). \quad (21)$$

Generally, processing path optimization algorithms can take two basic strategies to solve this extended task:

- Independently optimize paths for each $\check{\sigma}_G \in \mathcal{G}$, to identify $\check{\sigma}_G^*$ retrospectively.
- Integrate the identification of $\check{\sigma}_G^*$ into the path optimization procedure.

Strategy (a) results in a straight forward procedure using a standard single-goal process path optimization algorithm for every structure in \mathcal{G} , while strategy (b) often requires adoptions of the standard single-target path optimization algorithm. If the optimization algorithm works online like the proposed approach and not on a priori process samples, the overall process efficiency is highly dependent on the number of interactions. In the case of real processes, this determines the processing time, energy, and tool wear. In the case of simulated processes, it determines the computational cost of the process simulation. Strategy (a) uses the maximum amount of resources by optimizing processing paths for each $\check{\sigma}_G \in \mathcal{G}$ independently. By integrating the identification of the optimally reachable structure into the optimization procedure, the algorithm focuses its resources early on target microstructures that are considered to be reachable and ignores target microstructures that are very likely unreachable. Therefore, we propose a *multi-equivalent goal* reinforcement learning approach, which follows strategy (b).

In the remainder of this section, we firstly propose a deep reinforcement learning approach to solve single-target structure-guided processing path optimization problems, as depicted in Figure 3, and then extend it to our multi-equivalent goal structure-guided processing path optimization approach.

B. SINGLE-GOAL STRUCTURE-GUIDED PROCESSING PATH OPTIMIZATION

A microstructure changing process can be described by the set of allowed processing steps $a \in A$, a set of process state descriptions $s \in S$ and a transition function $P(s_{t+1}|s_t, a_t)$. The state description s_t at time step t consists of a representation $\mathfrak{d}(\sigma_t)$ of the associated microstructure σ_t and in

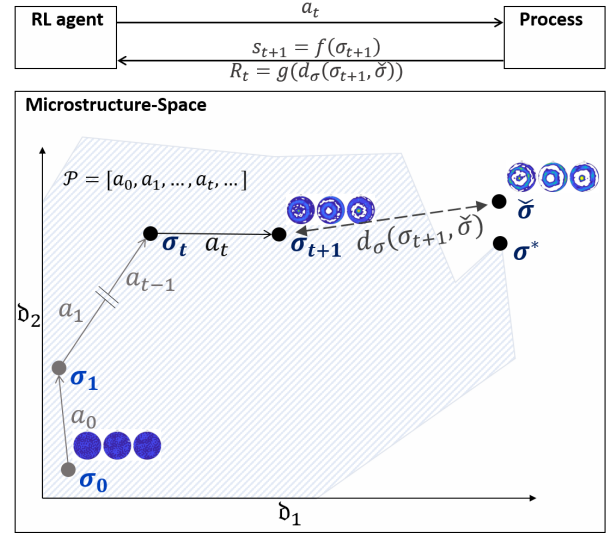


FIGURE 3. Schematic overview of single-goal structure-guided processing path optimization. For the target microstructure $\check{\sigma}$, the task is to find a path of process actions $\mathcal{P} = [a_0, a_1, \dots]$ that produces a microstructure σ^* , close to $\check{\sigma}$. The process is a black-box for the reinforcement learning agent. After executing a_t the process emits a state description s_{t+1} and a reward signal $R_{t+1} \in \mathbb{R}$. The reinforcement learning agent is structure-guided in the sense that s_t is a description of the microstructure σ_t and the reward-signal R_t is a function g of the microstructure distance $d_\sigma(\sigma_{t+1}, \check{\sigma})$. The region of reachable microstructures is depicted by the shaded area. Here, microstructures are represented by the crystallographic texture, depicted by 100, 110, and 111 pole figure plots.

some cases of additional process-state related quantities, like process-conditions or external process parameters. For the process studied in this paper, the microstructure is represented by truncated *generalized spherical harmonics*, thus $\mathfrak{d}(\sigma_t) = \zeta_t^\Omega(\sigma_t)$. The transition function P is not defined in an explicit form but can be sampled by interacting with the microstructure changing process or the process simulation.

To complete the formulation of the structure-guided processing path optimization as a Markov decision process (S, A, P, R, γ) , a reward function R and discount factor γ is needed. The proposed reward-formulation is based on a distance function d_σ , defined in the space of microstructure descriptors. Based on d_σ , a reward function which is in accordance with the formulation of the optimization objective \mathcal{P}^* is given as

$$R(s_t, a_t, s_{t+1}) = \begin{cases} \frac{1}{d_\sigma(\sigma_K, \check{\sigma})}, & \text{if } t = K - 1 \\ 0 & \text{, else,} \end{cases} \quad (22)$$

where σ_K is the microstructure associated with the terminal state s_K at the last time step K and where $\check{\sigma}$ denotes the target microstructure. Under this formulation exactly one non-zero reward signal is emitted per episode on the transition from s_{K-1} to s_K . If $\gamma = 1.0$, the expected future reward $V(s)$ for any state $s \in S$ indicates the expected inverse distance of the associated microstructure σ to the target microstructure $\check{\sigma}$ at the end of the episode.

Under this formulation, non-zero rewards are only occurring at the end of an episode. Especially for long process-paths (high values of K) this can lead to sample-inefficient learning due to the so-called *credit assignment problem* [14] when using unmodified RL algorithms like deep Q-Learning. An efficient way to deal with this problem is *potential-based reward shaping* as introduced in [24]. In order to get a dense reward signal for learning, the original reward function R is substituted by

$$R' = R + F, \quad (23)$$

where the shaping function F is in the form

$$F(s_t, s_{t+1}) = \gamma \Phi(s_{t+1}) - \Phi(s_t), \quad (24)$$

and $\Phi : S \rightarrow \mathbb{R}_0^+$ is a potential function of states $s \in S$. As proven in [24], the optimal policy π^* and near optimal policies are invariant to the substitution of R by R' for finite-horizon MDPs with a single terminal state. For problems with various terminal states \bar{S} the invariance is only guaranteed if $\Phi(\bar{s}) = 0$ for all potential terminal states $\bar{s} \in \bar{S}$ (compare [41], [42]). In our case, \bar{S} consists of all states that are reached at the end of the episodes. For all other cases, we use the inverse distance of the associated microstructure to the target microstructure as potential. Thus,

$$\Phi(s_t) = \begin{cases} 0 & , \text{if } t = K, \\ \frac{1}{d_\sigma(\sigma_t, \check{\sigma})} & , \text{else.} \end{cases} \quad (25)$$

After substituting (22), (24) and (25) into (23), the shaped reward function $R'(s_t, a_t, s_{t+1})$ is defined by

$$\begin{aligned} R' &= \begin{cases} \frac{1}{d_\sigma(\sigma_K, \check{\sigma})} + \gamma \Phi(s_K) - \Phi(s_t) & , \text{if } t = K - 1, \\ \gamma \Phi(s_{t+1}) - \Phi(s_t) & , \text{else,} \end{cases} \\ &= \begin{cases} \frac{1}{d_\sigma(\sigma_{t+1}, \check{\sigma})} - \frac{1}{d_\sigma(\sigma_t, \check{\sigma})} & , \text{if } t = K - 1, \\ \frac{\gamma}{d_\sigma(\sigma_{t+1}, \check{\sigma})} - \frac{1}{d_\sigma(\sigma_t, \check{\sigma})} & , \text{else.} \end{cases} \end{aligned} \quad (26)$$

For undiscounted MDPs, where $\gamma = 1.0$, the cases coincide to $R' = \frac{1}{d_\sigma(\sigma_{t+1}, \check{\sigma})} - \frac{1}{d_\sigma(\sigma_t, \check{\sigma})}$.

In opposition to R , R' emits a dense reward signal for every step during optimization. Due to the policy invariance, R' can be used as a substitute for R without narrowing the structure-guided processing path optimization result.

The single-goal structure-guided processing path optimization problem can be solved by a broad range of MDP solving approaches. Surrogate process models of different kinds representing $P(s_{t+1}|s_t, a_t)$ can be estimated from simulation samples as a basis for model-based optimization with dynamic programming methods. This approach would lead to a trade-off between sample-size and accuracy of the surrogate model and hence of the optimization result. In this context, it is important to notice that data acquisition from microstructure evolution simulations is usually computationally expensive. We propose to use model-free reinforcement

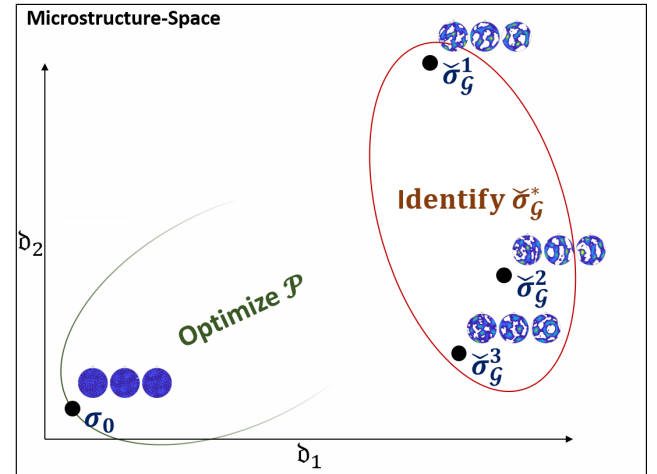


FIGURE 4. Schematic overview of multi-equivalent goal structure-guided processing path optimization. For a set of equivalent target microstructures $\mathcal{G} = \{\check{\sigma}_\mathcal{G}^1, \check{\sigma}_\mathcal{G}^2, \check{\sigma}_\mathcal{G}^3\}$ the objective is to identify the best reachable target microstructure $\check{\sigma}_\mathcal{G}^*$ from \mathcal{G} , while optimizing the processing path \mathcal{P} . Here, microstructures are represented by the crystallographic texture, depicted by 100, 110, and 111 pole figure plots.

learning algorithms that directly interact with the simulation model and thereby integrate sampling into the optimization process. Due to its sample-efficiency and the good performance on a broad range of tasks, we regard *deep Q networks* (DQN) as a good basis for structure-guided processing path optimization. For an increased sample efficiency and learning stability, we use *prioritized experience replay* [19], *double Q-Learning* [20], and *dueling Q-Learning* [21] extensions of DQN in our *structure-guided processing path optimization* approaches. Instead of the original reward, we learn expected values of the shaped reward function from (26). Like in the original DQN paper [18] we choose the initial exploration fraction ϵ_0 to linearly approach ϵ_f during the first n_ϵ episodes. The state-space S , the action-space A , and parameters used for our studies are further specified in Section IV.

C. MULTI-EQUIVALENT GOAL STRUCTURE-GUIDED PROCESSING PATH OPTIMIZATION

The multi-equivalent goal processing path optimization task differs from the single-goal task as depicted in Figure 4. Instead of a single target microstructure $\check{\sigma}$, a set \mathcal{G} of equivalent target microstructures $\check{\sigma}_\mathcal{G}^g \in \mathcal{G}$ is given. The definition of σ^* from (20) then extends to (21). As before \mathcal{P}^* is a processing-path leading from σ_0 to σ^* . However, to find \mathcal{P}^* , it is now required to also find the best reachable target microstructure $\check{\sigma}_\mathcal{G}^*$.

Because $\check{\sigma}_\mathcal{G}^*$ is not known, the reward function from (22) and the shaped reward function from (26) can not be applied directly to the multi-equivalent goal case. Following [22], a per-target pseudo reward function $R_g(s_t, a_t, s_{t+1})$ is defined. The per-target shaped reward function $R'_g(s_t, a_t, s_{t+1})$ is derived as described in (26). R_g and R'_g are the multi-target versions of (22) and (26), where $\check{\sigma}$ is replaced by the target

microstructure $\check{\sigma}_{\mathcal{G}}^g \in \mathcal{G}$. Also the optimal policy π^* now depends on $\check{\sigma}_{\mathcal{G}}^g$. The state-space S , the action-space A and the transition probabilities are independent of $\check{\sigma}_{\mathcal{G}}^g$ and remain unchanged.

The basis of our multi-equivalent goal approach is to define value functions that generalize over targets $\check{\sigma}_{\mathcal{G}}^g$, as proposed for the multi-goal reinforcement learning case in [22]. The state value function is thus formed by modifying the state value function \mathcal{V}_{π} from (1) into

$$\mathcal{V}_{g,\pi}(s_t) = \mathbb{E}_{P,\pi} \left[R_g(s_t, a_t, s_{t+1}) + \gamma \mathcal{V}_{g,\pi}(s_{t+1}) \right] \quad (27)$$

and the optimal state value function becomes $\mathcal{V}_g^* = \mathcal{V}_{g,\pi_g^*}$. Accordingly the state-action value function \mathcal{Q}_{π} becomes $\mathcal{Q}_{g,\pi}$ and the *double Q-learning* advantage function \mathcal{A}_{π} is $\mathcal{A}_{g,\pi}$, with $\mathcal{Q}_g^* = \mathcal{Q}_{g,\pi_g^*}$ and $\mathcal{A}_g^* = \mathcal{A}_{g,\pi_g^*}$.

As done in the single-goal approach, we use the extended *deep Q-Learning* algorithm for value-function approximation. The generalization of the estimated values across multiple targets is enabled by generalizing the single-goal function approximators during the approximation of the target dependent value functions. The optimal Q-function \mathcal{Q}_g^* is approximated by $\mathcal{Q}'(s, a, \mathfrak{d}(\check{\sigma}_{\mathcal{G}}^g), \theta)$ with model parameters θ , where $\mathfrak{d}(\check{\sigma}_{\mathcal{G}}^g)$ returns a feature vector of the target microstructure $\check{\sigma}_{\mathcal{G}}^g$. The extensions described in Section II-B can be applied directly to the generalized deep Q-learning approach. When using *dueling Q-learning*, \mathcal{V}_g^* is approximated by $\mathcal{V}'(s, \mathfrak{d}(\check{\sigma}_{\mathcal{G}}^g), \theta)$, and \mathcal{A}_g^* by $\mathcal{A}'(s, a, \mathfrak{d}(\check{\sigma}_{\mathcal{G}}^g), \theta)$ accordingly.

As described above, the major aim of the proposed multi-equivalent goal approach is to prioritize promising targets from \mathcal{G} during optimization and thereby enable a tractable processing path optimization. We use the expected distance of the terminal microstructure σ_K to the target microstructure $\check{\sigma}_{\mathcal{G}}^g$ as criterion for target-prioritization at the beginning of each episode. The state value $\mathcal{V}_g^*(s_0)$ of the original reward formulation (22) can be used to prioritize targets $\check{\sigma}_{\mathcal{G}}^g$ because it reflects the inverse of the expected distance of σ_K to $\check{\sigma}_{\mathcal{G}}^g$. However, due to reward shaping, we learn the optimal state value for the shaped reward function $\mathcal{V}'_g(s)$ instead. When $\Phi(s_K) = 0$ for every terminal state s_K , following [24], the relation between $\mathcal{V}_g^*(s)$ and $\mathcal{V}'_g(s)$ is

$$\mathcal{V}'_g(s) = \mathcal{V}_g^*(s) - \Phi(s). \quad (28)$$

Thus, we can reconstruct $\mathcal{V}_g^*(s_0)$ by

$$\mathcal{V}_g^*(s_0) = \mathcal{V}'_g(s_0) + \frac{1}{d_{\sigma}(\sigma_0, \check{\sigma}_{\mathcal{G}}^g)} \quad (29)$$

and on this basis estimate the best reachable target microstructure by

$$\check{\sigma}_{\mathcal{G}}^g = \arg \max_{\check{\sigma}_{\mathcal{G}}^g \in \mathcal{G}} \left[\mathcal{V}'(s_0, \mathfrak{d}(\check{\sigma}_{\mathcal{G}}^g), \theta) + \frac{1}{d_{\sigma}(\sigma_0, \check{\sigma}_{\mathcal{G}}^g)} \right], \quad (30)$$

where \mathcal{V}' is the approximated state value for the shaped rewards and $\mathfrak{d}(\check{\sigma}_{\mathcal{G}}^g)$ is the description of $\check{\sigma}_{\mathcal{G}}^g$.

As for the choice of processing actions during learning, we decide for a targeted $\check{\sigma}_{\mathcal{G}}$ per episode in an ϵ -greedy manner. Per episode, the target microstructure $\check{\sigma}_{\mathcal{G}} \in \mathcal{G}$ is chosen by

$$\check{\sigma}_{\mathcal{G}} = \begin{cases} \check{\sigma}_{\mathcal{G}}^g & , \text{ if } u > \epsilon^G, \\ \text{random}(\mathcal{G}) & , \text{ else,} \end{cases} \quad (31)$$

where $u \sim \mathcal{U}(0, 1)$ is randomly drawn from the uniform distribution over $[0, 1]$ and $\text{random}(\mathcal{G})$ returns a random sample from \mathcal{G} . The goal selection exploration rate ϵ^G is decoupled from the action selection exploration rate ϵ . The initial ϵ^G linearly approaches ϵ^G during the first n_{ϵ^G} episodes.

Inspired by the multi-goal augmentation in *hind-sight experience replay* [23], we add experience-tuples $(s_t, a, R_g, s_{t+1}, \mathfrak{d}(\check{\sigma}_{\mathcal{G}}^g))$ for all targets from \mathcal{G} with the associated potential reward to the replay memory \mathcal{D} , independently of the current target microstructure. Thereby, we further increase the sample-efficiency of our multi-equivalent goal approach.

The overall multi-equivalent goal approach is outlined in Listing 1. At the beginning of each episode, the episode target $\check{\sigma}_{\mathcal{G}}$ is picked in an ϵ^G -greedy manner (lines 2 and 3). For the sake of simplicity, we condense the per-episode execution of *multi-goal DQN* in line 4. By *multi-goal DQN* we denote the DQN algorithm combined with models that generalize over target microstructure descriptions $\mathfrak{d}(\check{\sigma}_{\mathcal{G}})$ as described above. The replay memory \mathcal{D} is not updated during the episode. Instead, the set of experience tuples from the current episode \mathcal{D}_e are returned by DQN. The replay memory \mathcal{D} is then updated by hypothetical experiences for all goals from \mathcal{G} (lines 5, 6, 9).

```
MEG-SGPPO(#episodes,  $\mathcal{G}$ ,  $\epsilon_0^G$ ,  $\epsilon_f^G$ ,  $n_{\epsilon}^G$ , DQNparameters)
1 for  $e = 1$  to #episodes
2    $\epsilon^G \leftarrow \max \left( \epsilon_f^G, \epsilon_0^G - \frac{e}{n_{\epsilon}^G} (\epsilon_0^G - \epsilon_f^G) \right)$ 
3    $\check{\sigma}_{\mathcal{G}} \leftarrow$  Eqs. (30), (31)
4    $\mathcal{D}_e \leftarrow$  execute multi-goal DQN w.  $\check{\sigma}_{\mathcal{G}}$  for one episode
5   for  $\check{\sigma}_{\mathcal{G}}^g \in \mathcal{G}$ 
6      $\mathcal{D}_e^g \leftarrow \{(s_t, a_t, s_{t+1}, R, \mathfrak{d}(\check{\sigma}_{\mathcal{G}}^g)) | (s_t, a_t, s_{t+1}, R) \in \mathcal{D}_e\}$ 
7     for  $(s_t, a_t, s_{t+1}, R, \tilde{g}) \in \mathcal{D}_e^g$ 
8        $R \leftarrow R'_g$  (Eq. 26), where  $\check{\sigma} = \check{\sigma}_{\mathcal{G}}^g$ 
9      $\mathcal{D} \leftarrow \mathcal{D} \cup \mathcal{D}_e^g$ 
```

Listing 1. Multi-equivalent-goal structure-guided processing path optimization.

IV. APPLICATION TO CRYSTALLOGRAPHIC TEXTURE EVOLUTION

A. ODF DISTANCE

For the reward functions defined in the previous section, a distance measure in microstructure space is required. In this contribution, we limit ourselves to crystallographic texture as the only microstructural feature to describe microstructures σ . To enable distance measurements between ODFs, we propose an orientation-histogram representation, achieved by

ODF binning in orientation-space. For the proposed histogram approach, a set of approximately equally sized bins in orientation space is required. Due to crystal symmetries, the orientation space can be reduced to a crystal symmetry dependent *fundamental zone*.

For a set of J orientations $o_j \in O_J^\Omega$, which are assumed to be equally distributed in the fundamental zone of a given crystal system Ω and an $SO(3)$ distance metric $\phi : SO(3) \times SO(3) \rightarrow \mathbb{R}_0^+$, we propose a nearest-neighbor bin assignment as is described in the following.

For a single crystal orientation h the assignment vector \mathbf{w}_h is defined by

$$\mathbf{w}_{h,j} = \begin{cases} 1 & , \text{if } o_j = \arg \min_{o \in O_J^\Omega} [\phi_\Omega(o, h)], \\ 0 & , \text{else,} \end{cases} \quad (32)$$

where $\mathbf{w}_{h,j}$ is the j -th vector component of \mathbf{w}_h and $\phi_\Omega : SO(3) \times SO(3) \rightarrow \mathbb{R}_0^+$ denotes the minimal distance ϕ for all equivalent orientations regarding Ω . Hence,

$$\phi_\Omega(o, h) = \min_{(\bar{o}, \bar{h}) \in \Psi_\Omega(o) \times \Psi_\Omega(h)} \phi(\bar{o}, \bar{h}), \quad (33)$$

where $\Psi_\Omega(h)$ is the set of all equivalent orientations of the orientation h for the crystal system Ω .

For a representative sample set H of orientations h and associated volume $V(h)$ from the crystallographic texture σ , the orientation histogram of σ is defined by the vector

$$\mathbf{b}_\sigma = \frac{1}{V} \sum_{h \in H} V(h) \cdot \mathbf{w}_h. \quad (34)$$

For any two crystallographic textures σ_a, σ_b , we then use the Chi-Square distance of the associated orientation histogram representations

$$\chi^2(\mathbf{b}_{\sigma_a}, \mathbf{b}_{\sigma_b}) = \sum_{j=0}^J \frac{(\mathbf{b}_{\sigma_a,j} - \mathbf{b}_{\sigma_b,j})^2}{(\mathbf{b}_{\sigma_a,j} + \mathbf{b}_{\sigma_b,j})} \quad (35)$$

as the distance function $d_\sigma(\sigma_a, \sigma_b)$.

We use $\phi(q_1, q_2) = \min(\|q_1 - q_2\|, \|q_1 + q_2\|)$ as basis distance function, where q_1, q_2 are orientations encoded as unit quaternions. ϕ is a metric in $SO(3)$ [43]. To generate the set of approximately uniformly distributed orientations O_J^Ω , we use the optimization based approach of Quey *et al.* [44]. For efficient nearest-neighbor queries, we use the *kd-tree* algorithm.

To smoothen the distance function, in practice we use a soft assignment $\tilde{\mathbf{w}}_h$ instead of the hard assigned weights \mathbf{w}_h from (32). $\tilde{\mathbf{w}}_h$ is defined by

$$\tilde{\mathbf{w}}_{h,i} = \begin{cases} \frac{\phi_\Omega(o_i, h)}{\sum_{o_j \in N} \phi_\Omega(o_j, h)} & , \text{if } o_i \in N, \\ 0 & , \text{else,} \end{cases} \quad (36)$$

where $N = \text{NN}_k(O_J^\Omega, h, \phi_\Omega)$ is the set of the k nearest neighbors of h from O_J^Ω . We study the effect of the parameters J and k on the ODF distance function and regarding the representation quality in Section V.

B. APPLICATION SCENARIO

To evaluate the proposed algorithms, a texture generating process based on the Taylor-type material model is set up. The process consists of subsequent steps of uniaxial tension or compression, variably oriented to the reference coordinate system of the material model. In each step, a deformation $\hat{\mathbf{F}}$ is applied:

$$\hat{\mathbf{F}} = \mathbf{R} \tilde{\mathbf{F}} \mathbf{R}^\top, \quad (37)$$

with a rotation defined by the matrix \mathbf{R} and

$$\tilde{\mathbf{F}} = \begin{bmatrix} \tilde{F}_{11} & 0 & 0 \\ 0 & F_{22} & 0 \\ 0 & 0 & F_{33} \end{bmatrix}. \quad (38)$$

While \tilde{F}_{11} is variable, F_{22} and F_{33} are determined by the simulation framework until the stresses are in balance.

The process parameters that have to be optimized are

- 1) the magnitude of \tilde{F}_{11}
- 2) the rotation matrix \mathbf{R}

After each process step, the reorientation of the single crystals is calculated based on the rigid body rotation \mathbf{R}_e , which follows from the polar decomposition of the elastic part of the deformation gradient \mathbf{F} [45]. To avoid unrealistically large deformations, the process is limited to induce 70% equivalent strain. Based on the reached crystallographic textures, material properties can be calculated such as Young's modulus E .

For the evaluation studies, a processing path consists of up to K subsequent process-steps. The per-step process control action $a_t = (f_t, \mathbf{q}_t)$ is composed of the deformation magnitude $f_t \in [-1.0, 1.0]$, representing \tilde{F}_{11} at process-step t and the rigid body rotation \mathbf{R} at processing-step t encoded as unit quaternion $\mathbf{q}_t \in \{x \in \mathbb{H} \mid \|x\|_2 = 1\}$. In our evaluation scenario, we restrict f_t to the interval $[-0.02, 0.02]$. For our value based deep reinforcement learning approaches, we discretize the action space A by setting $f \in \{0.02, -0.02\}$ and $\mathbf{q} \in O_{100}$, where O_{100} is a set of 100 nearly uniformly distributed unit quaternions. Furthermore, the action space contains a *no-op* action to be used when no further improvement regarding the distance to the goal microstructure during the episode is expected.

The state-space S consists of descriptions of reachable microstructures. As microstructures σ are described by the according ODF, states $s \in S$ are represented by ODF descriptors. For this purpose we use truncated *generalized spherical harmonics* coefficients ζ_ℓ^Ω , as introduced in Section II-D. We truncate the series at $\ell = 8$. For the used material with cubic crystal symmetry, the ODF is represented by 21 independent complex-valued coefficients. In addition to the GSH microstructure description, the state vector s contains the current time-step and equivalent strain.

C. IMPLEMENTATION DETAILS

Single goal evaluation optimization runs consist out of 100 subsequent process episodes with a maximal length of $K =$

100 each. The initial microstructure state is a uniform orientation distribution (often also called grey texture) and consists of 250 equally weighted orientations which are nearly uniformly distributed in the fundamental zone of the cubic crystal symmetry. If not stated otherwise for specific results, experiments are conducted with the following hyperparameters:

- d_σ as defined in (35) with histogram parameters $J = 512$ and $k = 3$.
- A discount factor of $\gamma = 1.0$.
- Deep Q-learning as described in Section II-B as basic algorithm where the target-network is updated every $n_\theta = 250$ time-steps.
- Prioritized replay as described in Section II-B, with $\alpha_{PER} = 0.6$ and $\beta_0 = 0.4$.
- Double-Q-learning and dueling-Q-learning as described in Section II-B.
- An ϵ -greedy policy. With an initial exploration rate $\epsilon_0 = 0.5$ and the final exploration-rate $\epsilon_f = 0.1$, with $n_\epsilon = 50$.
- Q-networks with hidden layer sizes of $[128, 64, 32]$, layer normalization and *ReLU* activation functions. The learning process starts after 100 control-steps. The networks are trained after each control-step with a mini-batch of size 32.
- ADAM is used as optimizer for neural network training, with a learning rate of $5e^{-4}$.

Multi equivalent goal optimization runs consist of 200 subsequent process episodes. Hyperparameters differ from the single goal experiments in the following points:

- Due to the higher data complexity we expanded the neural network to 4 hidden layers of sizes $[128, 256, 256, 128]$.
- Per time-step the network is trained with four mini-batches instead of one.
- For improved stability, we reduced the target-network update frequency to $n_\theta = 500$ steps.
- Exploration parameters are $\epsilon_0 = 0.5$ and the final exploration-rate $\epsilon_f = 0.0$, with $n_\epsilon = 190$. The ϵ -greedy target choice is parametrized with $\epsilon_0^G = 1.0$, $\epsilon_f^G = 0.0$, $n_\epsilon^G = 190$.

The Tailor-type material model and the simulation framework are implemented in Fortran. The reinforcement learning code is implemented in python. The reinforcement learning environment code supports the *openAI gym* interface [27]. Reinforcement learning agents are implemented based on *stable baselines*, an open-source collection of implementations of deep reinforcement learning algorithms. The *sciPy* *kdtree* implementation is used for orientation distribution representation calculations [46]. *Neper* [47] is used to generate the approximately uniformly distributed orientations following the approach from [44]. Approximately uniformly distributed orientations are used to define the bins of the orientation histogram described in Section III, the initial texture for our experiments, and the discrete action-space as

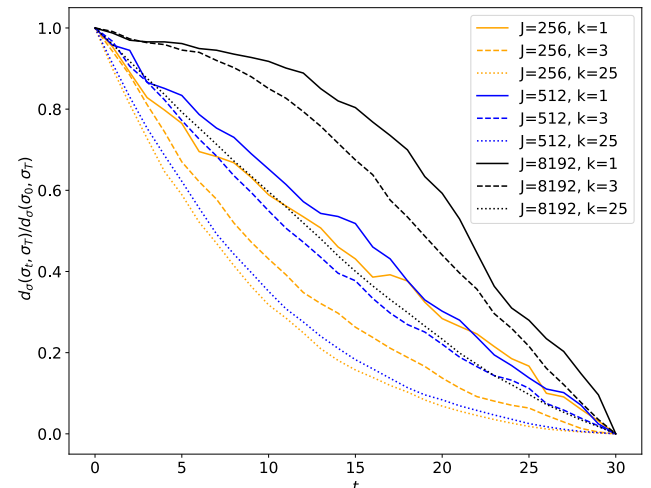


FIGURE 5. Comparison of the effect of orientation histogram parameters on the resulting ODF distance function. Relative distance $d_\sigma(\sigma_t, \sigma_K)/d_\sigma(\sigma_0, \sigma_K)$ over t for an exemplary process with static process parameters, where σ_t is the microstructure at time-step t and σ_K is the microstructure resulting from the process.

described in this Section. Experiments have been conducted on workstations with 20 2.2 GHz CPU cores (mainly used by the simulation) and GTX 1080 Ti GPUs (for artificial neural network training).

V. RESULTS AND DISCUSSION

A. ORIENTATION HISTOGRAM PARAMETERS

The ODF distance is represented by the distance between orientation histograms as presented in IV. A. The effect of the histogram formation parameters J (number of histogram bins) and k (soft assignment neighborhood size) on the ODF distance function is shown in Figure 5. For various (J, k) -settings and an exemplary process path of the distance to the crystallographic texture σ_T in relation to the initial distance $d_\sigma(\sigma_t, \sigma_T)/d_\sigma(\sigma_0, \sigma_T)$ is plotted over time steps t . The exemplary process path is sampled from the process described in Section IV-B by starting from a uniform ODF and applying a constant deformation in direction $q = (1, 0, 0, 0)$ for 30 process steps. When constantly approaching σ_T as in the exemplary process path, a monotone decreasing distance function is assumed in the reward function formulations ((22) and (26)). For $k = 1$ (solid lines) the distance-trajectory is not strictly monotone. A clear smoothing effect, depending on the soft assignment parameter k , can be observed.

TABLE 2. Mean absolute error of Young's modulus E in 11, 22 and 33 direction for various orientation histogram parameters J, k in GPa

J	k		
	1	3	25
256	574	238	401
512	493	201	275
8192	196	77	57

The information loss induced by the orientation histogram

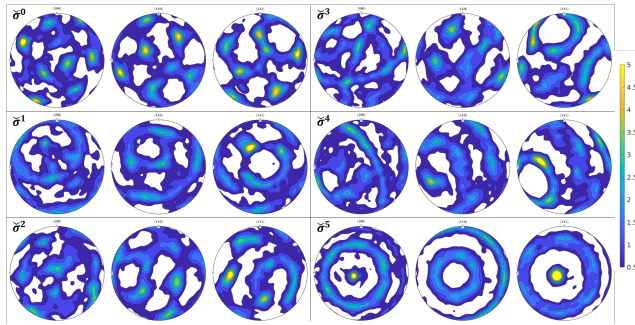


FIGURE 6. Pole figure triples of the target-textures from G , used throughout the single-goal studies. Miller indices of the pole figures from left to right: [100, 110, 111]

representation of the ODF can be seen from the effect on the material properties. Table 2 lists the mean error of Young's modulus induced by the discretization and smoothing for various parameters (J, k). The mean absolute errors are calculated based on 1000 crystallographic textures which are randomly sampled from a set of textures reachable by the process and by calculating Young's modulus for the original texture and the orientation histogram of the texture. While increasing the number of bins, J has a clear and monotone positive impact regarding the mean absolute error in both cases. An adequate soft-assignment parameter for the sampled crystallographic textures in our search-grid is $k = 3$. The computational cost of the nearest-neighbor search is highly effected by J . A reasonable hyperparameter setting, which we use throughout our studies, is ($J = 512, k = 3$).

B. SINGLE-GOAL PROCESSING PATH OPTIMIZATION

A set of six target textures is used throughout the evaluation of the single goal algorithm: $G = \{\check{\sigma}^0, \check{\sigma}^1, \check{\sigma}^2, \check{\sigma}^3, \check{\sigma}^4, \check{\sigma}^5\}$. The textures are visualized in Figure 6 in the form of pole figures. The calculated properties for the sampled target-textures are listed in Table 3. The six target textures have been randomly sampled from a set of textures, which are likely reachable by the process. The following criteria have been applied to guarantee the diversity of the sample:

- 1) $d_\sigma(\check{\sigma}^i, \check{\sigma}^j) > 1.2$ for all $\check{\sigma}^i, \check{\sigma}^j$ in G .
- 2) $\min_{\hat{\sigma} \in G} d_\sigma(\check{\sigma}, \hat{\sigma}) > 0.75$, where $\hat{\sigma}$ is the uniform ODF.

TABLE 3. Young's modulus of target textures from G in GPa

Goal	E_{11}	E_{22}	E_{33}
$\check{\sigma}^0$	221	223	221
$\check{\sigma}^1$	216	221	212
$\check{\sigma}^2$	223	219	214
$\check{\sigma}^3$	222	218	223
$\check{\sigma}^4$	224	218	219
$\check{\sigma}^5$	227	226	233

The single goal algorithm is applied to each target microstructure from G separately. The solution variety (due to stochastic exploration and function approximation) has been

covered by multiple independent optimization runs of 100 reinforcement learning episodes each. The learning objective is to find a processing path from the initial microstructure close to the target microstructure $\check{\sigma}$.

During learning, each episode ends after K time-steps or when the equivalent-strain exceeds its limit of 70%. Processing paths can be pruned in hindsight. The optimal sub-path of episode e regarding the optimization task is the path from the initial microstructure σ_0 to $\check{\sigma}_e = \arg \min_{\sigma \in \mathcal{S}_e} d_\sigma(\sigma, \check{\sigma})$, where $\mathcal{S}_e \subset S$ is the set of microstructures on the processing path of episode e . The mean distance of $\check{\sigma}_e$ to the according target microstructure per episode is plotted for three independent optimization runs per goal-microstructure from G on the left of Figure 7 together with the per-target 95% confidence intervals. On the right of Figure 7 the goal-distance of the current best processing path is plotted over episodes.

Qualitative results of a single exemplary optimization run are shown on the left of Figure 8. On the right of Figure 8, the results for a single episode are shown. The visualized results belong to the best of the three independent optimization runs with the target microstructure $\check{\sigma}^0$. On the left, the goal-distance of the current best processing path is plotted for the single optimization run as in Figure 7 with pole figures of $\check{\sigma}_0, \check{\sigma}_4, \check{\sigma}_{10}, \check{\sigma}_{21}, \check{\sigma}_{40}$ and the resulting microstructure of the best found processing path $\check{\sigma}_{97}$. On the upper right, the associated target microstructure $\check{\sigma}^0$ is visualized. On the right of Figure 8 the processing path of episode 97 is plotted in the form of a scatter plot, where the control action displacement direction (vertical axis) is plotted along with the displacement sign (color) against the processing time-step number. Additionally, the distance of the microstructures within the episode σ_t to the target microstructure $\check{\sigma}^0$ is plotted as a line plot. Each dot in the scatter plot represents an action $a_t \in A$, where the positions on the y-axis mark the chosen load orientation $q \in O_{100}$ and the colors mark the chosen load. The dashed vertical line marks the time-step of the best microstructure of the episode $\check{\sigma}_{97}$ in terms of the distance to the target microstructure. The solid vertical line marks the end of the episode, in this case, due to the equivalent load criterion. Figure 9 shows the best found processing path of all optimization run for all target microstructures from G in the top row and pole figures of the corresponding processing path results in the middle row, and below the processing path result of the worst optimization run for the corresponding target microstructure. Figure 9 in combination with Figure 7 shows, that for some microstructures ($\check{\sigma}^3, \check{\sigma}^5$) the processing paths are composed of only very few different actions, which are found in the first few episodes.

Figure 10 shows ablation study results on target microstructure $\check{\sigma}^0$ for the single goal algorithm. Per setting the mean and 95% confidence interval is plotted for three independent optimization runs. The plot shows that the addition of the three DQN extensions, namely *Prioritized Experience Replay*, *Double Q-Learning*, *Dueling Q-Learning*, has no major impact on the optimization outcome but slightly stabilizes and accelerates the convergence. The results of the

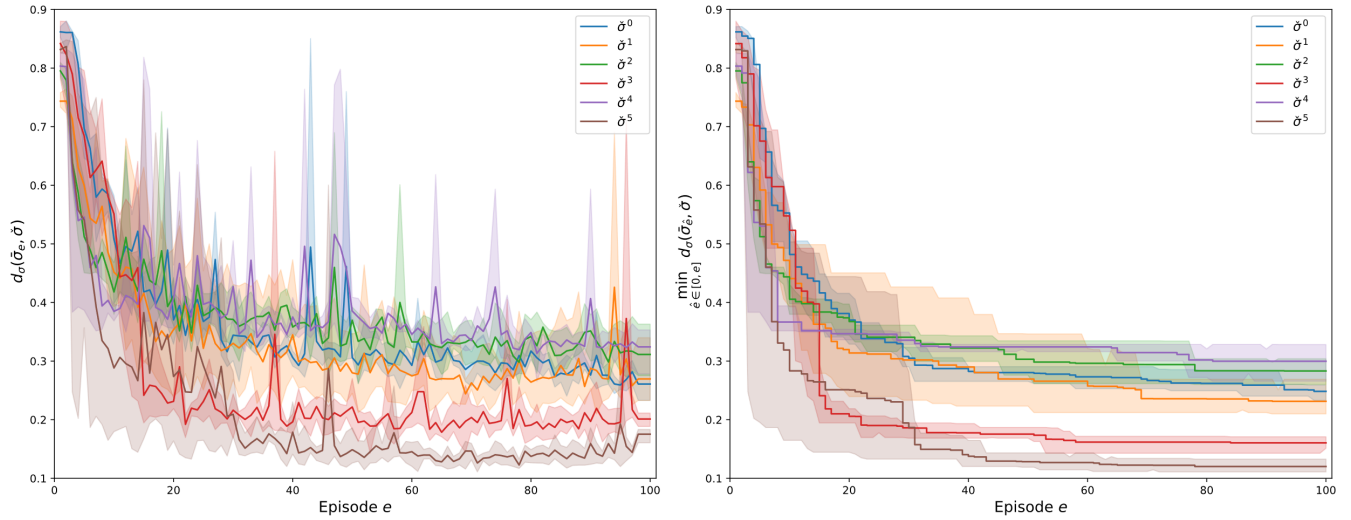


FIGURE 7. Single-goal reinforcement learning results for the microstructure goals G . (left) The mean and the 95% confidence interval of the goal-distance of $\bar{\sigma}$ per episode e and $\bar{\sigma} \in G$ (color). (right) Shortest previous goal-distance during the optimization run.

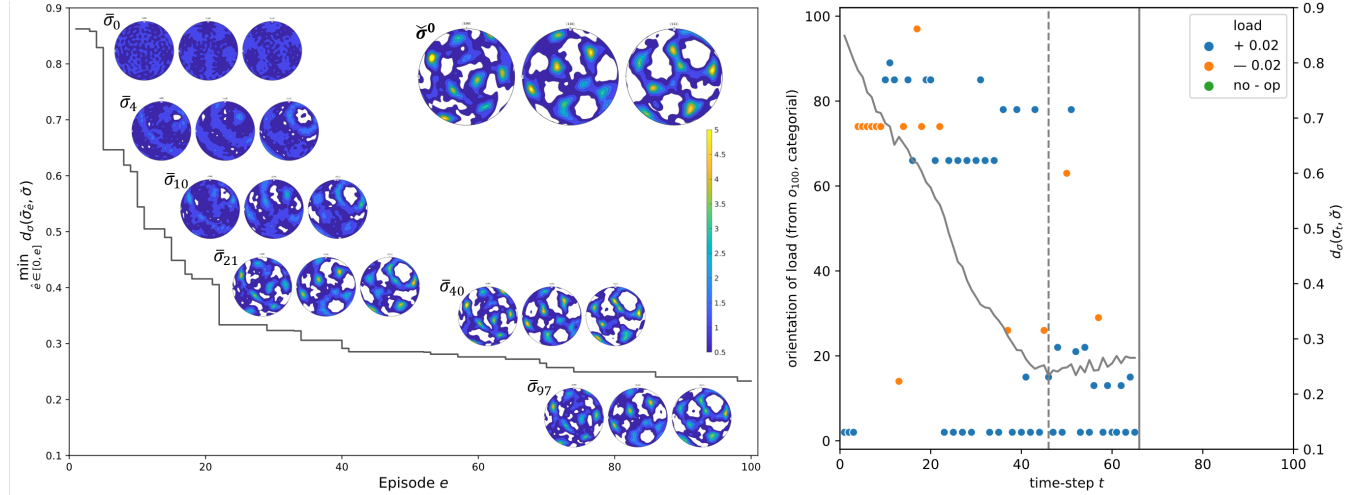


FIGURE 8. Single-goal optimization. (left) Best optimization run for $\bar{\sigma}^0 \in G$ with pole figure plots. Miller indices of the pole figures from left to right: [100, 110, 111]. (right) Episode 97 of the exemplar optimization run with control actions and the goal-distance visualized per time-step.

single goal algorithm with the pure reward signal from (22) (green curve) reveals the impact of reward shaping on the convergence speed, and hence on the data efficiency of the algorithm.

C. MULTI-EQUIVALENT GOAL PROCESSING PATH OPTIMIZATION

According to the results reported in the previous subsection, especially for $\bar{\sigma}^2$ and $\bar{\sigma}^4$ no satisfactory processing paths were found by the single-goal algorithm. Contrary to the single-goal approach, the multi-equivalent goal optimization approach aims to reach one of several target microstructures that are equivalent with respect to the material properties. In this subsection, we report and discuss the results of the multi-equivalent goal structure-guided processing path optimization (MEG-SGPPO) algorithm as introduced in Section

III-C. To study the advantages of the multi-equivalent goal approach we sampled target microstructure sets $\mathcal{G}^{\sigma^4\text{-equiv}}$ and $\mathcal{G}^{\sigma^2\text{-equiv}}$, where $\mathcal{G}^{\sigma^4\text{-equiv}}$ consists of 10 distinctive $\bar{\sigma}^4$ -equivalent microstructures $\bar{\sigma}_{4\text{-equiv}}^g$ and $\mathcal{G}^{\sigma^2\text{-equiv}}$ of 10 distinctive $\bar{\sigma}^2$ -equivalent microstructures $\bar{\sigma}_{2\text{-equiv}}^g$. For this purpose, we defined a microstructure $\bar{\sigma}_{k\text{-equiv}}^g$ to be equivalent to $\bar{\sigma}^k \in G$ if the Young's modulus $E_{jj}(\bar{\sigma}_{k\text{-equiv}}^g)$ are within a range of $+/- 0.5$ GPa of $E_{jj}(\bar{\sigma}^k)$ for $j \in 1, 2, 3$.

The results of MEG-SGPPO on $\mathcal{G}^{\sigma^4\text{-equiv}}$ and $\mathcal{G}^{\sigma^2\text{-equiv}}$ are visualized in Figure 11. In both cases, we conducted one optimization run and present quantitative results per-episode and qualitative results for the best episodes in the bottom row. As in Figure 8 (left), the distance of nearest structure $\bar{\sigma}_e$ to the actual chosen target structure from the set $\mathcal{G}^{\sigma\text{-equiv}}$ is plotted per episode e . The per-episode target

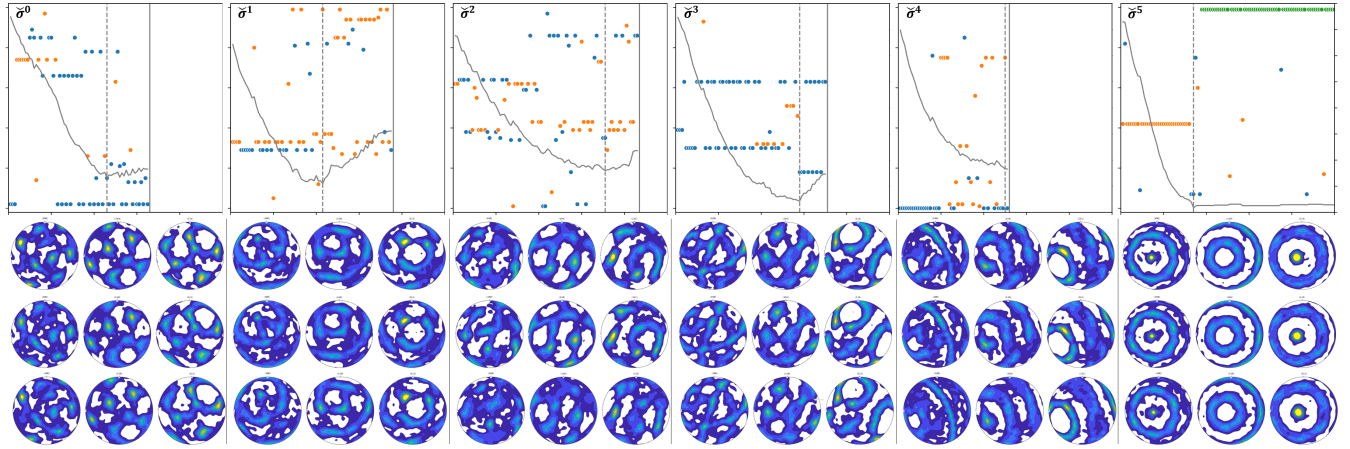


FIGURE 9. Single goal reinforcement learning results per target microstructure $\check{\sigma} \in G$. (top) Best found processing path per target microstructure (plot axis parameters are identical to Figure 8, right). (bottom) Three lines of per-target [100, 110, 111] pole figures. First line: target microstructures from G . Second line: resulting microstructures of the best found processing paths in the best of the three independent optimization runs. Third line: resulting microstructures of the best found processing paths in the worst of the three independent optimization runs

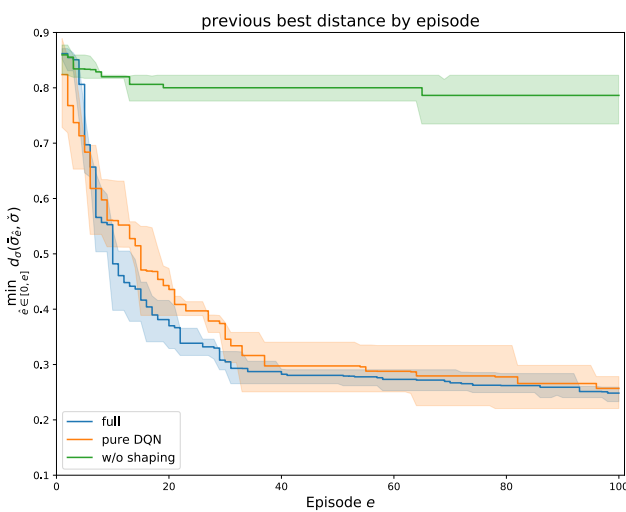


FIGURE 10. Ablation results (mean and 95% confidence interval) for $\check{\sigma}^0$. Best previous goal distance by episode for three independent optimization runs each of various settings. Blue: results of the full featured algorithm as reported in 7, orange: pure DQN (without *Prioritized Experience Replay, Double Q-Learning, Dueling Q-Learning*), green: results obtained without reward-shaping.

microstructure choice of the algorithm is depicted by the color of the respective scatter dot. The type of the specific selection (explorative/greedy) is represented by the shape of the respective scatter dot. Due to the decreasing goal-picking exploration factor ϵ^G , the variety of the targeted microstructures is high in the beginning and then decreases during the learning process.

As the scatter plot for $\mathcal{G}^{\sigma^4\text{-equiv}}$ (Figure 11 (left)) and the underlying pole figure plots of $\check{\sigma}^1_{4\text{-equiv}}$ suggest, this target microstructure is closer to the grey texture than the other equivalent targets from $\mathcal{G}^{\sigma\text{-equiv}}$. Although the algorithm finds good processing paths for other target microstructures ($\check{\sigma}^0_{4\text{-equiv}}$ and $\check{\sigma}^8_{4\text{-equiv}}$), it rapidly commits to $\check{\sigma}^1_{4\text{-equiv}}$ due to

the low distance $d_\sigma(\sigma_0, \check{\sigma}^1_{4\text{-equiv}})$, and does not change this target in the greedy episodes during the experiment. In the case of $\mathcal{G}^{\sigma^2\text{-equiv}}$ (Figure 11 (right)), the algorithm tries to find a good processing path for $\check{\sigma}^6_{2\text{-equiv}}$ during the first 105 episodes. After obtaining better results for $\check{\sigma}^3_{2\text{-equiv}}$ in episode 103 the greedy target fluctuates between $\check{\sigma}^3_{2\text{-equiv}}$ and $\check{\sigma}^6_{2\text{-equiv}}$. After episode 144 the algorithm finally decides for $\check{\sigma}^3_{2\text{-equiv}}$ due to the repeating better results for $\check{\sigma}^3_{2\text{-equiv}}$ after episode 103 compared to $\check{\sigma}^6_{2\text{-equiv}}$.

The best result obtained during the single-goal approach experiments for the respective original microstructure (0.2656 for $\check{\sigma}^4$, 0.2601 for $\check{\sigma}^2$) is depicted as a baseline by the grey dashed line in Figure 11, top-left and top-right. This baseline is exceeded by MEG-SGPO during the first 25 episodes for $\mathcal{G}^{\sigma^4\text{-equiv}}$ and during the first 75 episodes for $\mathcal{G}^{\sigma^2\text{-equiv}}$. In both cases, the algorithm yields notably better results during the 200 episodes than the single goal approach does on the original target microstructure.

On the bottom of Figure 11, qualitative results are plotted for the best episodes of the best reached target microstructure ($\check{\sigma}^1_{4\text{-equiv}}$ in Figure 11 (left), and $\check{\sigma}^3_{2\text{-equiv}}$ in Figure 11 (right)) and the second best reached target microstructure ($\check{\sigma}^0_{4\text{-equiv}}$ in Figure 11 (left) and $\check{\sigma}^6_{2\text{-equiv}}$ in Figure 11 (right)). For each of the four qualitative results, we show on the left the pole figures of the target texture and below the pole figures of the resulting texture of the best found processing path $\check{\sigma}_e$. Right of the pole figures, the best found processing path is shown in form of a scatter plot of the chosen action per processing step and - overlaid as a line chart - the corresponding microstructure distance to the respective target microstructure. The pole figures give an impression of the similarity between the results and the respective target structures. The according process diagrams show the complexity of the found processes while approaching the process targets.

To investigate the benefit of the proposed multi-goal augmentation, we conducted repeated optimization runs with and

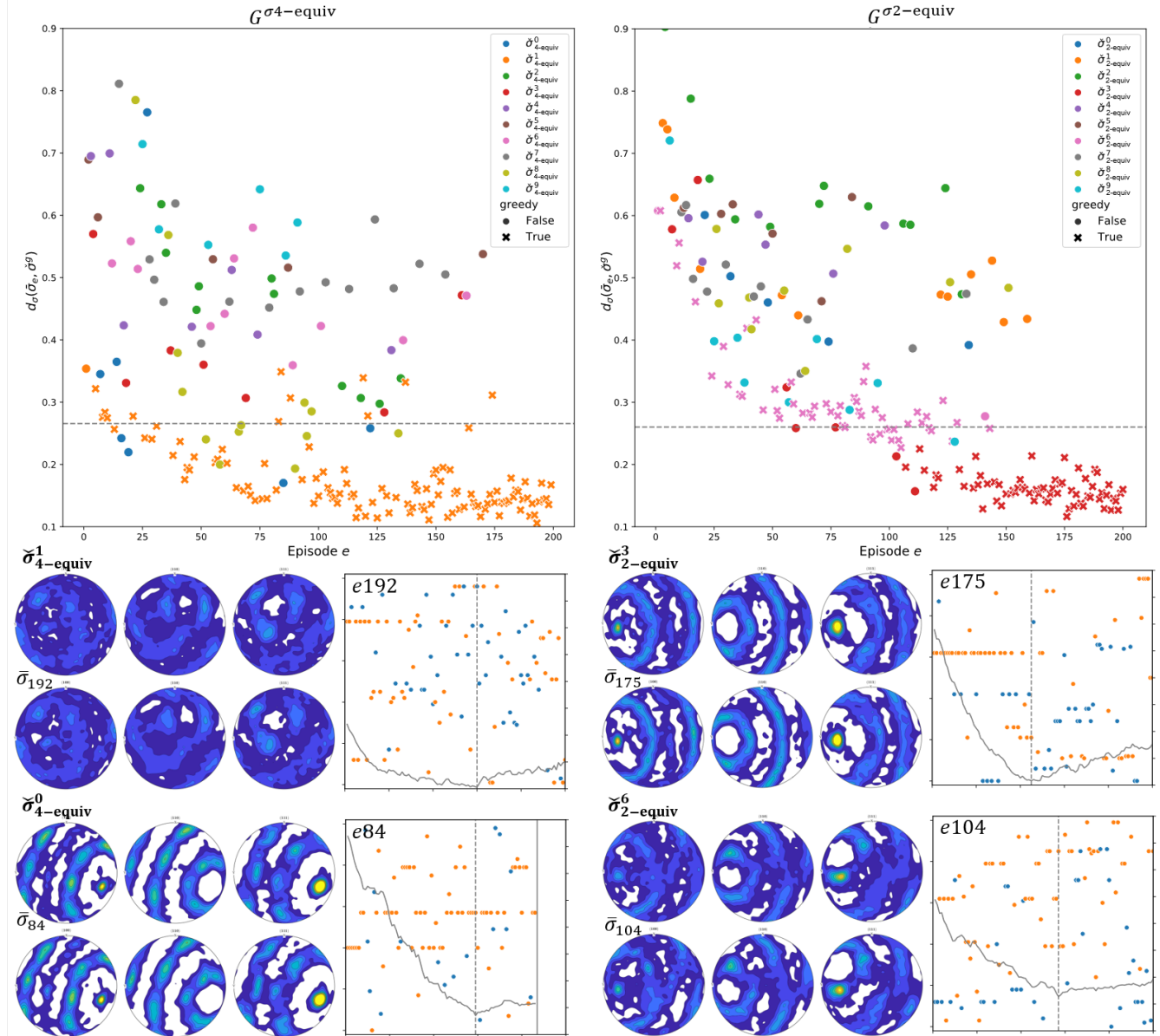


FIGURE 11. Results of the multi-equivalent goal algorithm for a set of 10 microstructures $\bar{\sigma}_k^g \in \mathcal{G}^{\sigma^4\text{-equiv}}$ equivalent to $\bar{\sigma}^4 \in G$ (left), and 10 microstructures $\bar{\sigma}_k^g \in \mathcal{G}^{\sigma^2\text{-equiv}}$ equivalent to $\bar{\sigma}^2 \in G$ (right). Top: Scatter-plots of the best distance to the selected target microstructure $d_\sigma(\bar{\sigma}_e, \bar{\sigma}_k^g)$ over episode numbers, where the dot color denotes the selected target microstructure per episode and the dot shape the type of the target microstructure selection. The best reached goal-distance to the respective original target microstructure from the single-goal experiments (0.2656 for $\bar{\sigma}^4 \in G$ and 0.2601 for $\bar{\sigma}^2 \in G$) is marked by a grey dashed line. Bottom: Qualitative results of the two microstructures closest to one of the equivalent target microstructures at the corresponding episode e for each of the two experiments: Pole figures of the texture of the chosen target $\bar{\sigma}_k^g$ and the nearest reached texture $\bar{\sigma}_e$ with its episode number e (projections 100, 110, 111, where the color map is identical to Figure 6). To the right of the pole figures the processing path of the episode e , according to $\bar{\sigma}_e$ is plotted. The plot axis parameters are identical to Figure 7 (right).

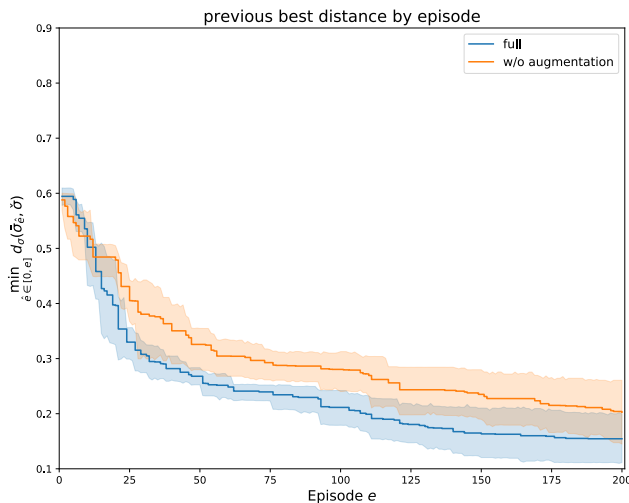


FIGURE 12. Ablation results (mean and 95% confidence interval) for the target microstructure set $\mathcal{G}^{\sigma^2\text{-equiv}}$. Best previous goal distance for episode for five independent optimization runs per setting. Blue: full featured approach, as introduced and used for other MEG-SGGPO results reported. Orange: without multi-goal augmentation.

without the use of this feature. In Figure 12, results for the MEG-SGGPO algorithm with and without the augmentation of the replay memory by data for non-pursued goals are depicted in the form of the best previous result plot known from the last subsection. Basis of the plot are five independent optimization runs with the full-featured MEG-SGGPO algorithm (blue) and three independent optimization runs without augmentation (orange) on the target-microstructure set $\mathcal{G}^{\sigma^2\text{-equiv}}$. As the plot suggests, the augmentation improves the overall optimization result.

VI. CONCLUSION AND OUTLOOK

In the present paper, two deep reinforcement learning approaches are proposed to solve processing path optimization problems with the objective function and state representation in the structure space. The *single-goal structure-guided processing path optimization* algorithm (SG-SGGPO) combines function-based reinforcement learning techniques and a reward shaping mechanism for structure-guided processing path optimization. However, from the materials design point of view, typically various microstructural compositions are equivalent concerning a desired macroscopic material property. Recent approaches for the inversion of structure-property linkages identify whole sets of optimal microstructures. The proposed single goal approach was therefore extended to form a *multi-equivalent-goal structure-guided processing path optimization* algorithm (MEG-SGGPO) for efficient optimization when multiple target microstructures are given. We applied both algorithms to a simulated metal forming process and used the orientation density function (ODF) to represent the state of the microstructures (in this example, the crystallographic texture). To apply our generic algorithms to the exemplary application, we introduced a

histogram-based ODF distance function.

In the result section of this paper, we report the results of a parameter study for the proposed ODF distance function and evaluation results of the algorithms SG-SGGPO and MEG-SGGPO applied to optimization problems on the metal forming process simulation. We show the probability of the multi-equivalent goal algorithm to early prioritize promising microstructures from a set of multiple equivalent targets. We investigate the usefulness of the central features of both algorithms in the form of ablation study results.

The MEG-SGGPO algorithm generalizes over target microstructures. This ability can further be used to transfer the learned process knowledge to other processes. The transfer can be performed by using the trained Q-models across optimization tasks, which differ by varying sets of equivalent optimal microstructures. The application of deep reinforcement learning algorithms to sequences of tasks often suffer from *catastrophic forgetting* (knowledge about previous tasks is overwritten by recent training iterations). The incorporation of techniques like *elastic weight consolidation* [48] into the multi-equivalent goal algorithm could help to overcome this problem.

The proposed algorithms are not restricted to applications with orientation density functions as microstructural features or applications in metal forming only. Due to the model-free nature of the approaches, the algorithms can be applied to any new application field or process if (a) the microstructure is observable during the process and (b) a distance function for the specific microstructure feature-space is defined.

The application to the optimization of simulated processes with more accurate microstructure descriptors (2-point statistics, full-field models) furthermore requires an improved computational efficiency of the underlying process simulation. As the fields of data-driven computational material sciences and numerical simulation progresses rapidly, we are confident that applications that are intractable by now become feasible in the upcoming years. Nevertheless, with our multi-equivalent goal approach and the capability to generalize over specific target microstructures, we address the need for data-efficient methods.

Although we used a deterministic process simulation to evaluate the proposed methods, they are suitable also for non-deterministic processes. In particular, the multi-equivalent goal prioritization is derived from the learned expectation functions. Thereby our methods are also applicable for processes with stochastic state transitions. Notably, it is possible to learn directly on physical processes without the need for any prior process knowledge if the according structure features are measurable at processing time.

REFERENCES

- [1] G. B. Olson, “Computational design of hierarchically structured materials,” *Science*, vol. 277, no. 5330, pp. 1237–1242, 1997.
- [2] R. Liu, A. Kumar, Z. Chen, A. Agrawal, V. Sundararaghavan, and A. Choudhary, “A predictive machine learning approach for microstructure optimization and materials design,” *Scientific Reports*, vol. 5, no. 1, pp. 1–12, 2015.

[3] A. Paul, P. Acar, W.-k. Liao, A. Choudhary, V. Sundararaghavan, and A. Agrawal, "Microstructure optimization with constrained design objectives using machine learning-based feedback-aware data-generation," *Computational Materials Science*, vol. 160, pp. 334–351, 2019.

[4] B. L. Adams, A. Henrie, B. Henrie, M. Lyon, S. Kalidindi, and H. Garmestani, "Microstructure-sensitive design of a compliant beam," *Journal of the Mechanics and Physics of Solids*, vol. 49, no. 8, pp. 1639–1663, 2001.

[5] D. T. Fullwood, S. R. Niezgoda, B. L. Adams, and S. R. Kalidindi, "Microstructure sensitive design for performance optimization," *Progress in Materials Science*, vol. 55, no. 6, pp. 477–562, 2010.

[6] J. B. Shaffer, M. Knezevic, and S. R. Kalidindi, "Building texture evolution networks for deformation processing of polycrystalline fcc metals using spectral approaches: Applications to design for targeted performance," *International Journal of Plasticity*, vol. 26, no. 8, pp. 1183–1194, 2010. [Online]. Available: <http://dx.doi.org/10.1016/j.ijplas.2010.03.010>

[7] D. Li, H. Garmestani, and B. Adams, "A texture evolution model in cubic-orthotropic polycrystalline system," *International Journal of Plasticity*, vol. 21, no. 8, pp. 1591–1617, 2005.

[8] D. Li, H. Garmestani, and S. Ahzi, "Processing path optimization to achieve desired texture in polycrystalline materials," *Acta Materialia*, vol. 55, no. 2, pp. 647–654, 2007.

[9] P. Acar and V. Sundararaghavan, "Linear solution scheme for microstructure design with process constraints," *AIAA Journal*, pp. 4022–4031, 2016.

[10] ———, "Reduced-order modeling approach for materials design with a sequence of processes," *AIAA Journal*, vol. 56, no. 12, pp. 5041–5044, 2018.

[11] S. Sundar and V. Sundararaghavan, "Database development and exploration of process-microstructure relationships using variational autoencoders," *Materials Today Communications*, 2020.

[12] A. Tran, J. A. Mitchell, L. Swiler, and T. Wilsey, "An active learning high-throughput microstructure calibration framework for solving inverse structure-process problems in materials informatics," *Acta Materialia*, 2020.

[13] H. Bunge and C. Esling, "Texture development by plastic deformation," *Scripta Metallurgica*, vol. 18, no. 3, pp. 191–195, 1984.

[14] R. S. Sutton and A. G. Barto, *Reinforcement learning: An introduction*. MIT press, 2018.

[15] Y. Ma, W. Zhu, M. G. Benton, and J. Romagnoli, "Continuous control of a polymerization system with deep reinforcement learning," *Journal of Process Control*, vol. 75, pp. 40–47, 2019.

[16] J. Günther, P. M. Pilarski, G. Helfrich, H. Shen, and K. Diepold, "Intelligent laser welding through representation, prediction, and control learning: An architecture with deep neural networks and reinforcement learning," *Mechatronics*, vol. 34, pp. 1–11, 2016.

[17] J. Dornheim, N. Link, and P. Gumbisch, "Model-free adaptive optimal control of episodic fixed-horizon manufacturing processes using reinforcement learning," *International Journal of Control, Automation and Systems*, pp. 1–12, 2019.

[18] V. Mnih, K. Kavukcuoglu, D. Silver, A. A. Rusu, J. Veness, M. G. Bellemare, A. Graves, M. Riedmiller, A. K. Fidjeland, G. Ostrovski et al., "Human-level control through deep reinforcement learning," *Nature*, vol. 518, no. 7540, pp. 529–533, 2015.

[19] T. Schaul, J. Quan, I. Antonoglou, and D. Silver, "Prioritized experience replay," *arXiv preprint arXiv:1511.05952*, 2015.

[20] H. Van Hasselt, A. Guez, and D. Silver, "Deep reinforcement learning with double q-learning," in *Thirtieth AAAI conference on artificial intelligence*, 2016.

[21] Z. Wang, T. Schaul, M. Hessel, H. Van Hasselt, M. Lanctot, and N. De Freitas, "Dueling network architectures for deep reinforcement learning," *arXiv preprint arXiv:1511.06581*, 2015.

[22] T. Schaul, D. Horgan, K. Gregor, and D. Silver, "Universal value function approximators," in *International conference on machine learning*, 2015, pp. 1312–1320.

[23] M. Andrychowicz, F. Wolski, A. Ray, J. Schneider, R. Fong, P. Welinder, B. McGrew, J. Tobin, O. P. Abbeel, and W. Zaremba, "Hindsight experience replay," in *Advances in Neural Information Processing Systems*, 2017, pp. 5048–5058.

[24] A. Y. Ng, D. Harada, and S. Russell, "Policy invariance under reward transformations: Theory and application to reward shaping," in *ICML*, vol. 99, 1999, pp. 278–287.

[25] F. Roters, P. Eisenlohr, L. Hantcherli, D. D. Tjahjanto, T. R. Bieler, and D. Raabe, "Overview of constitutive laws, kinematics, homogenization and multiscale methods in crystal plasticity finite-element modeling: Theory, experiments, applications," *Acta Materialia*, vol. 58, no. 4, pp. 1152–1211, 2010.

[26] P. Eisenlohr, M. Diehl, R. A. Lebensohn, and F. Roters, "A spectral method solution to crystal elasto-viscoplasticity at finite strains," *International Journal of Plasticity*, vol. 46, pp. 37–53, 2013.

[27] G. Brockman, V. Cheung, L. Pettersson, J. Schneider, J. Schulman, J. Tang, and W. Zaremba, "Openai gym," *arXiv preprint arXiv:1606.01540*, 2016.

[28] C. J. C. H. Watkins and P. Dayan, "Q-learning," *Machine Learning*, vol. 8, no. 3-4, pp. 279–292, 1992.

[29] L.-J. Lin, "Self-improving reactive agents based on reinforcement learning, planning and teaching," *Machine learning*, vol. 8, no. 3-4, pp. 293–321, 1992.

[30] S. Thrun and A. Schwartz, "Issues in using function approximation for reinforcement learning," in *Proceedings of the 1993 Connectionist Models Summer School* Hillsdale, NJ. Lawrence Erlbaum, 1993.

[31] S. R. Kalidindi, C. A. Bronkhorst, and L. Anand, "Crystallographic texture evolution in bulk deformation processing of fcc metals," *Journal of the Mechanics and Physics of Solids*, vol. 40, no. 3, pp. 537–569, 1992.

[32] H. P. Frederikse, "Elastic constants of single crystals," *Handbook of Chemistry and Physics*, vol. 12, pp. 33–38, 2008.

[33] J. R. Rice, "Inelastic constitutive relations for solids: An internal-variable theory and its application to metal plasticity," *Journal of the Mechanics and Physics of Solids*, vol. 19, no. 6, pp. 433–455, 1971.

[34] R. J. Asaro and A. Needleman, "Overview no. 42 texture development and strain hardening in rate dependent polycrystals," *Acta Metallurgica*, vol. 33, no. 6, pp. 923–953, 1985.

[35] H. Zhang, M. Diehl, F. Roters, and D. Raabe, "A virtual laboratory using high resolution crystal plasticity simulations to determine the initial yield surface for sheet metal forming operations," *International Journal of Plasticity*, vol. 80, pp. 111–138, 2016.

[36] M. Baiker, D. Helm, and A. Butz, "Determination of mechanical properties of polycrystals by using crystal plasticity and numerical homogenization schemes," *Steel Research International*, vol. 85, no. 6, pp. 988–998, 2014.

[37] J. Pagenkopf, A. Butz, M. Wenk, and D. Helm, "Virtual testing of dual-phase steels: Effect of martensite morphology on plastic flow behavior," *Materials Science and Engineering: A*, vol. 674, pp. 672–686, 2016.

[38] C. Tome, G. R. Canova, U. F. Kocks, N. Christodoulou, and J. J. Jonas, "The relation between macroscopic and microscopic strain hardening in f.c.c. polycrystals," *Acta Metallurgica*, vol. 32, no. 10, pp. 1637–1653, 1984.

[39] J. Pagenkopf, "Bestimmung der Plastischen Anisotropie von Blechwerkstoffen durch ortsaufgelöste Simulationen auf Gefügeebene," Ph.D. dissertation, Fakultät für Maschinenbau des Karlsruher Instituts für Technologie (KIT), 2019.

[40] H.-J. Bunge, *Texture analysis in materials science: mathematical methods*. Elsevier, 2013.

[41] M. Grześ, "Reward shaping in episodic reinforcement learning," in *Proceedings of the 16th Conference on Autonomous Agents and MultiAgent Systems*, ser. AAMAS '17. ACM, 2017, p. 565–573.

[42] P. M. Mannion, S. Devlin, K. Mason, J. Duggan, and E. Howley, "Policy invariance under reward transformations for multi-objective reinforcement learning," *Neurocomputing*, vol. 263, pp. 60–73, 2017.

[43] D. Q. Huynh, "Metrics for 3D rotations: Comparison and analysis," *Journal of Mathematical Imaging and Vision*, vol. 35, no. 2, pp. 155–164, 2009.

[44] R. Quey, A. Villani, and C. Maurice, "Nearly uniform sampling of crystal orientations," *Journal of Applied Crystallography*, vol. 51, no. 4, pp. 1162–1173, 2018.

[45] X. Ling, M. Horstemeyer, and G. Potirniche, "On the numerical implementation of 3d rate-dependent single crystal plasticity formulations," *International Journal for Numerical Methods in Engineering*, vol. 63, no. 4, pp. 548–568, 2005.

[46] P. Virtanen, R. Gommers, T. E. Oliphant, M. Haberland, T. Reddy, D. Cournapeau, E. Burovski, P. Peterson, W. Weckesser, J. Bright et al., "Scipy 1.0: fundamental algorithms for scientific computing in python," *Nature Methods*, pp. 1–12, 2020.

[47] R. Quey, P. Dawson, and F. Barbe, "Large-scale 3d random polycrystals for the finite element method: Generation, meshing and remeshing," *Computer Methods in Applied Mechanics and Engineering*, vol. 200, no. 17–20, pp. 1729–1745, 2011.

[48] J. Kirkpatrick, R. Pascanu, N. Rabinowitz, J. Veness, G. Desjardins, A. A. Rusu, K. Milan, J. Quan, T. Ramalho, A. Grabska-Barwinska et al., "Overcoming catastrophic forgetting in neural networks," *Proceedings of the national academy of sciences*, vol. 114, no. 13, pp. 3521–3526, 2017.

• • •